MOLECULAR BIOLOGY

HMGB1 deforms nucleosomal DNA to generate a dynamic chromatin environment counteracting the effects of linker histone

Hayden S. Saunders[1,2], Un Seng Chio[1]†, Camille M. Moore[1,2,3]†, Vijay Ramani[1,3], Yifan Cheng[1,4], Geeta J. Narlikar[1]*

The essential architectural protein HMGB1 increases accessibility of nucleosomal DNA and counteracts the effects of linker histone H1. However, HMGB1 is less abundant than H1 and binds nucleosomes more weakly, raising the question of how it competes with H1. Here, we find that HMGB1 increases nucleosomal DNA accessibility without displacing H1. HMGB1 also increases the dynamics of condensed, H1-bound chromatin. Unexpectedly, cryo–electron microscopy structures show HMGB1 bound at internal locations on nucleosomes and local DNA distortion. These sites are away from where H1 binds, explaining how HMGB1 and H1 can co-occupy a nucleosome. Our findings suggest a model where HMGB1 counteracts the effects of H1 by distorting nucleosomal DNA and disrupting interactions of the H1 carboxyl-terminal tail with DNA. Compared to mutually exclusive binding, co-occupancy by HMGB1 and H1 allows greater diversity in dynamic chromatin states. More generally, these results explain how architectural proteins acting at the nucleosome scale can have large effects on chromatin dynamics at the mesoscale.

INTRODUCTION

In eukaryotes, the fundamental unit of chromatin is a nucleosome, which is composed of ~147 base pair (bp) of DNA wrapped around an octamer of histone proteins. Nucleosome formation typically inhibits access to DNA for processes such as transcription, replication, or DNA repair (*1*). It is well known that adenosine 5′-triphosphate (ATP)–dependent chromatin remodelers facilitate access to nucleosomal DNA (*2*). There also exist ATP-independent mechanisms that regulate the intrinsic dynamics of nucleosomal DNA through the actions of architectural proteins (*3*–*9*). In mammalian cells, the two most abundant architectural proteins, HMGB1 (high mobility group box 1) and linker histone H1, regulate chromatin through opposing effects (*10*). While the expression of HMGB1 is correlated with chromatin decompaction and transcriptional activation, the presence of H1 is associated with chromatin compaction and transcriptional repression (*8*, *11*–*13*). Examples of transitions from HMGB1-bound chromatin to H1-bound chromatin have been observed during *Xenopus* and *Drosophila* embryonic development (*14*, *15*). Further, H1 turnover dynamics have been shown to be sensitive to HMGB1 concentration in vivo (*16*). In stem cells, where HMGB1 is most highly expressed, H1 turns over more rapidly compared to differentiated cells (*17*, *18*). These results imply that the relative activities of HMGB1 and H1 are critical for defining cell identity. Despite the biological significance, the molecular basis for how HMGB1 and H1 counteract each other's activities is not known.

In current models, it has been proposed that HMGB1 and H1 directly compete because they bind nucleosomes in a mutually exclusive manner near the entry/exit site of DNA (*10*, *15*, *16*, *19*, *20*). However, even at its highest expression level, HMGB1 is present in the nucleus at 10-fold lower concentration and has ~1000-fold weaker affinity for nucleosomes and shorter residence times on chromatin than H1 (*21*–*31*). These differences raise the question of how HMGB1 effectively competes with H1 for the same binding site. In addition, several structures exist of linker histones bound to nucleosomes, which explain how H1 inhibits nucleosomal DNA unwrapping (*31*–*33*). In comparison, there are no structures of HMGB1 bound to nucleosomes because its weak affinity for nucleosomes and high dissociation rates make it difficult to capture stable structures. A better understanding of how HMGB1 interacts with and perturbs nucleosome structure will enable a deeper understanding of how HMGB1 and H1 compete.

What is known about HMGB1's interaction with the nucleosome is based on synthesizing careful studies with a variety of substrates. The mammalian HMGB1 consists of two HMG box domains, which bind DNA without sequence specificity. Each box contains two hydrophobic residues that intercalate into the minor groove of DNA and induce a bend in the DNA (*9*). HMGB1 also contains a C-terminal autoinhibitory domain consisting of 30 consecutive negatively charged Asp and Glu residues, which mimics DNA to occlude the DNA binding interface of the HMG boxes (Fig. 1A) (*34*–*36*). Therefore, DNA bound by HMGB1 is in competition with the autoinhibitory C-terminal tail, resulting in a high off rate and low affinity (*28*, *35*). These binding and bending dynamics are how HMGB1 lowers the persistence length of DNA to make it more flexible (*37*). In addition, the autoinhibition of HMGB1's C-terminal tail is relieved by interaction with the H3 tail (*26*, *38*, *39*). This work has led to the hypothesis that HMGB1 promotes unwrapping of nucleosomal DNA using its ability to bend DNA (*39*–*41*). Yeast (Hmo1 and Nhp6) and *Drosophila* (HMG-D) homologs of HMGB1 partially unwrap nucleosomal DNA (*42*, *43*). H1 also relieves HMGB1's autoinhibition via direct interaction of their respective C-terminal tails, raising questions about a direct competition model (*19*). However, to date, competition between HMGB1 and H1 has not been studied in vitro on mononucleosomes, so other modes of competition have not been tested.

[1]Department of Biochemistry and Biophysics, University of California, San Francisco, San Francisco, CA 94158, USA. [2]Tetrad Graduate Program, University of California, San Francisco, San Francisco, CA 94158, USA. [3]Gladstone Institute for Data Science and Biotechnology, San Francisco, CA 94158, USA. [4]Howard Hughes Medical Institute, University of California, San Francisco, San Francisco, CA 94158, USA.
*Corresponding author. Email: geeta.narlikar@ucsf.edu
†These authors contributed equally to this work.

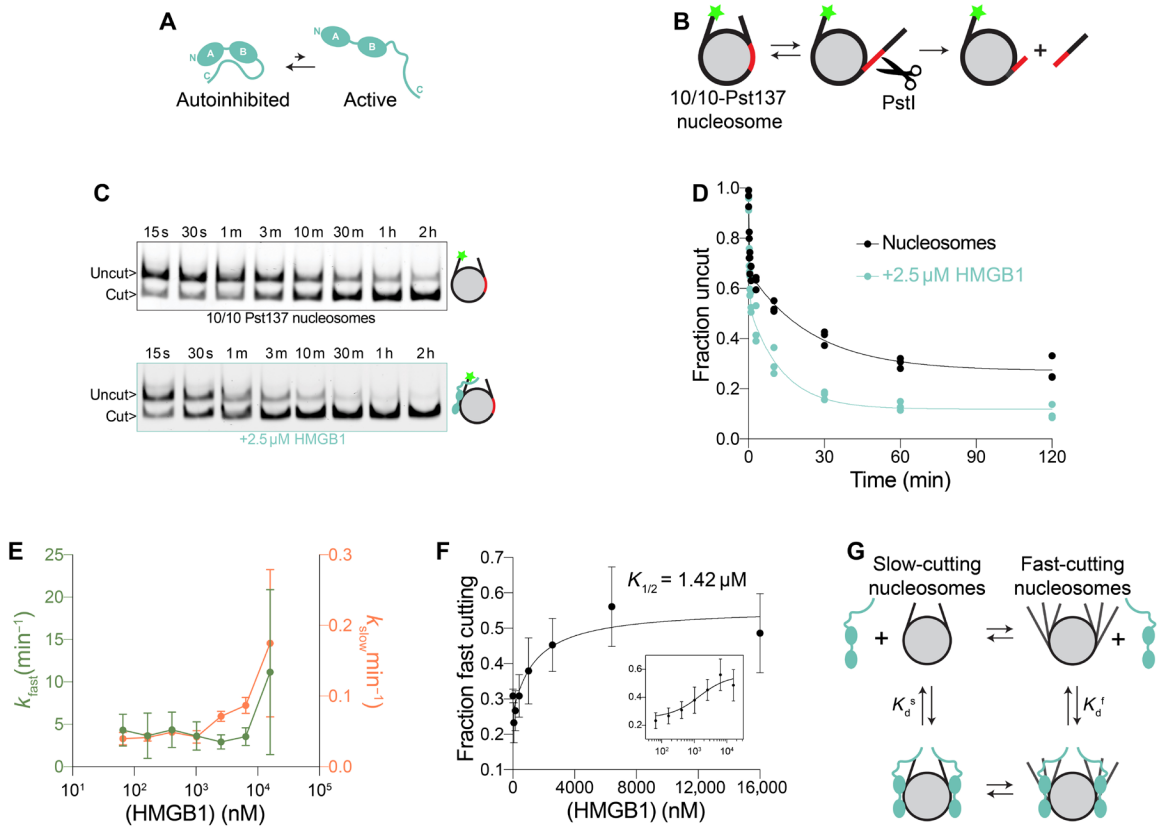

Fig. 1. HMGB1 grants access to nucleosomal DNA. (**A**) A schematic of autoinhibition of HMGB1's DNA binding A and B boxes by the negatively charged C-terminal tail. (**B**) A schematic of the REA assay showing how nucleosomal DNA cutting by the restriction enzyme PstI occurs when nucleosomal DNA transiently unwraps from the octamer core. The green star represents the fluorescent label on the end of the DNA. (**C**) Representative gels of time courses of REA on 10/10-Pst137 nucleosomes with (bottom) and without (top) the presence of 2.5 μM HMGB1. PstI cleavage results in the appearance of the lower, cut band over time. m, minutes. h, hours. (**D**) Quantification of three replicate experiments of (B). The fraction of DNA that remains uncut is plotted as a function of time. The data for all three replicates are fit by a two-step exponential decay function. (**E**) Rate constants (k_{fast} and k_{slow}) for REA experiments on 10/10-Pst137 nucleosomes are shown as a function of HMGB1 concentration. Error bars represent the SD for three separate replicates. (**F**) The fraction of nucleosomes that are described by k_{fast} is plotted as a function of HMGB1 concentration. Error bars represent the SD for three separate replicates. Curve represents a fit by an equation derived from the model in (G). An overall half-maximal concentration of HMGB1 for its effect is 1.42 μM ($K_{1/2}$). Inset shows the same plot with a logarithmic *x* axis. (**G**) A schematic of a model showing a slow and a fast-cutting population of nucleosomes that interconvert slowly relative to the timescale of PstI cutting and are bound by HMGB1 with different affinities. K_d^s is 2.4 μM while K_d^f is 650 nM. K_ds are derived from the equations in Materials and Methods.

Here, to obtain a molecular understanding of how HMGB1 and H1 influence each other's activities, we study their impact on reconstituted mononucleosomes and nucleosomal arrays. Using a quantitative assay to measure the transient unwrapping of nucleosomal DNA and cryo–electron microscopy (cryo-EM) to determine the first structures of HMGB1 on nucleosomes, we find that HMGB1 and H1 do not compete for binding. Rather, our data suggest that HMGB1 binds and deforms DNA at multiple sites along the nucleosomal and flanking DNA, counteracting H1's inhibition of DNA accessibility without displacing it. We further show that HMGB1 increases the dynamics of H1 bound to condensed chromatin and of H1-bound chromatin itself. Overall, our findings provide a structural explanation for how HMGB1 affects nucleosomal DNA and offer a molecular mechanism for how HMGB1 and H1 counter each other's activities to regulate chromatin dynamics at the atomic and mesoscales. This mechanism, based on binding and conformational equilibria, represents a distinct and ATP-independent mechanism for regulating global chromatin accessibility and dynamics.

RESULTS

Quantitative assay to measure impact of HMGB1 on nucleosomal DNA unwrapping

Previous studies have shown that HMG box–containing proteins enhance unwrapping of nucleosomal DNA (*42*–*44*). To quantitatively test how human HMGB1 affects this process, we adapted a restriction enzyme accessibility (REA) assay, which has been used to measure intrinsic DNA unwrapping within a nucleosome (*7*). In this assay, a restriction enzyme site is placed within the nucleosomal DNA and the transient unwrapping of DNA from the octamer core is measured by the rate of restriction enzyme cutting (Fig. 1B). DNA unwrapping preferentially occurs near the entry/exit sites of nucleosomal DNA, where fewer histone-DNA interactions need to be disrupted to make the DNA accessible (*3*). Given that HMGB1 has been hypothesized to bind near the entry exit site (*15*, *20*), we used nucleosomes with 10 bp of flanking DNA on either side of the Widom 601 nucleosome positioning sequence, which was modified to contain a PstI restriction enzyme site centered at position 137

(10/10-Pst137; Fig. 1B). We find that restriction enzyme cleavage is enhanced in the presence of HMGB1 (Fig. 1, C and D), consistent with HMGB1's role in increasing DNA unwrapping.

It has previously been shown that HMGB1 prefers the presence of flanking DNA to interact with nucleosome substrates (*21*, *26*). To assess whether flanking DNA is also essential for HMGB1's effect on nucleosomal DNA unwrapping, we performed REA assays on nucleosomes with asymmetric flanking DNA (0/10 or 10/0). We found that HMGB1 enhances restriction enzyme cutting on both substrates (fig. S1, A and B). Although nucleosomal DNA is slightly less accessible when there is no flanking DNA proximal to the PstI cut site (10/0-Pst137, fig. S1B), HMGB1 still enhances restriction enzyme cutting on these nucleosomes. This suggests that HMGB1 enhances the existing unwrapping dynamics of nucleosomal DNA.

These results prompted us to look more closely at how exactly HMGB1 interacts with nucleosome substrates. In electrophoretic mobility shift–based binding experiments using fluorescently end-labeled nucleosomes, HMGB1 produces two up-shifted bands (fig. S2A). The two bands are consistent with a 2:1 stoichiometry of HMGB1 on nucleosomes. This two-step binding pattern is observed when HMGB1 binds symmetric 10/10 and asymmetric 0/10 nucleosomes (fig. S2A), suggesting that symmetric flanking DNA is dispensable for HMGB1's stoichiometry. In addition, there is minimal effect on nucleosome affinity when removing one half of the flanking DNA, while removing all flanking DNA causes a 10-fold decrease in affinity (fig. S2, B and C). The observed higher affinity for nucleosomes with longer-flanking DNA (fig. S2C) likely arises because increasing the length of flanking DNA generates HMGB1-binding sites that resemble those on naked DNA. Yet, HMGB1 still promotes detectable enhancement of DNA unwrapping on core nucleosomes (fig. S1C). Overall, these results suggest that while flanking DNA increases the affinity of HMGB1 for nucleosomes, by providing additional higher affinity binding sites, flanking DNA is not essential for HMGB1's activity on nucleosomal DNA, suggesting that other interactions with the nucleosome also facilitate HMGB1's activity.

It is known that the HMGB1 C-terminal tail interacts with the histone H3 N-terminal tail (*26*, *38*, *39*). It is also known that the H3 tail interacts with nucleosomal DNA and inhibits DNA accessibility (*45*, *46*). Therefore, it has been hypothesized that the interaction between the HMGB1 C-terminal tail and the H3 tail could result in sequestration of the H3 tail and relief of autoinhibition by HMGB1's C-terminal tail, both of which would increase HMGB1's ability to unwrap DNA (*39*). However, the H3-tail interaction may also provide an additional anchor to localize HMGB1 to a nucleosome. To test this possibility, we deleted the C-terminal tail of HMGB1 (HMGB1-ΔC). HMGB1-ΔC does not yield the two-step nucleosome-binding pattern of wild-type (WT) HMGB1 and instead binds nonspecifically at a much higher stoichiometry and affinity (fig. S2A). In addition, HMGB1-ΔC inhibits restriction enzyme cutting (fig. S3, A and B), likely due to steric inhibition by the HMG boxes bound nonspecifically to nucleosomal DNA. We also tested the effect of deleting the H3 N-terminal tail (ΔH3tail). Consistent with the H3 tail's role in inhibiting access to nucleosomal DNA, we saw a marked increase in restriction enzyme cutting, which was not further increased by HMGB1 (fig. S4, A and B). These results raise the possibility that interaction between the HMGB1 C-terminal tail and the histone H3 N-terminal tail localizes HMGB1 near the entry/exit site in addition to relieving autoinhibition.

HMGB1 selectively stabilizes a nucleosome conformation with exposed nucleosomal DNA

In all REA experiments, we observe that nucleosomal DNA cutting contains two kinetic phases, suggesting that nucleosomes exist in two conformations that interconvert more slowly than cutting by PstI. In this model, one of the conformations is cut more rapidly (fast-cut) than the other (slow-cut), with respective rate constants of k_{fast} and k_{slow}. k_{fast} is similar to the rate constant of cutting naked DNA (fig. S3, D and E), suggesting that the fast-cut conformation has nucleosomal DNA at position 137 that is fully accessible to PstI. The fast-cut population is not due to contaminating free DNA as we do not detect substantial free DNA in our assembled nucleosomes (fig. S3C).

To investigate how HMGB1 influences these populations of nucleosomes, we performed REA at a range of HMGB1 concentrations and compared the rate constants of the fast- and slow-cut populations (k_{fast} and k_{slow}) as a function of HMGB1 concentration (fig. S1, D and E). To our surprise, we found that the magnitude of k_{fast} or k_{slow} was not substantially dependent on the concentration of HMGB1 (Fig. 1E). Instead, the fraction of nucleosomes that were cut fast increased with increasing concentrations of HMGB1 (Fig. 1F), indicating that at higher HMGB1 concentrations, a greater population of nucleosomes has more accessible DNA. The increase in the fast-cut fraction as a function of HMGB1 concentration resembles a binding curve (Fig. 1F), implying that HMGB1 binding correlates with an increase in the population of fast-cutting nucleosomes. To quantify this effect, we fit a model to the data whereby HMGB1 binds the fast-cut nucleosomes more strongly than the slow-cut nucleosomes, resulting in a shift in the equilibrium toward the fast-cut population when nucleosomes are fully bound by HMGB1 (Fig. 1G). This analysis revealed that HMGB1 has a roughly fourfold-binding preference for fast-cut over slow-cut nucleosomes (Fig. 1G). In addition, the analysis showed that 50% of HMGB1's stimulatory effect on nucleosomal DNA unwrapping occurred at ~1.4 μM, a $K_{1/2}$ value that is comparable to the dissociation constant (K_d) measured for HMGB1 to 10/10 nucleosomes (fig. S2C). Overall, these results are consistent with a model where HMGB1 increases nucleosomal DNA accessibility by preferentially stabilizing fast-cut nucleosomes.

Cryo-EM structures of HMGB1 bound to nucleosomes imply transient interactions at multiple sites

To date, there are structures of HMGB1 bound to DNA but no structures of HMGB1 bound to nucleosomes (*47*, *48*). A key challenge in capturing nucleosome bound structures is the weak affinity of HMGB1. While cross-linking is often used to stabilize weak chromatin-binding proteins for cryo-EM, we wanted to preserve any effects of HMGB1 on nucleosome dynamics. Therefore, we optimized the cryo-EM protocol to visualize how HMGB1 interacts with a nucleosome without cross-linking. We collected a cryo-EM dataset of 0/10 nucleosomes bound by HMGB1. Despite HMGB1's low affinity to this substrate, we were able to determine a three-dimensional (3D) reconstruction where we detect one HMG box bound directly to the nucleosomal DNA at superhelical location −2 (SHL −2) (Fig. 2, A and B, and figs. S5 and S6). Unexpectedly, unlike previous data predicting HMGB1 to interact near the entry/exit site (*15*, *20*), we see HMGB1 interacting directly with the nucleosome at an internal site. This position is notably similar to recent cryo-EM structures of the related transcription factors (TFs) SOX2 and

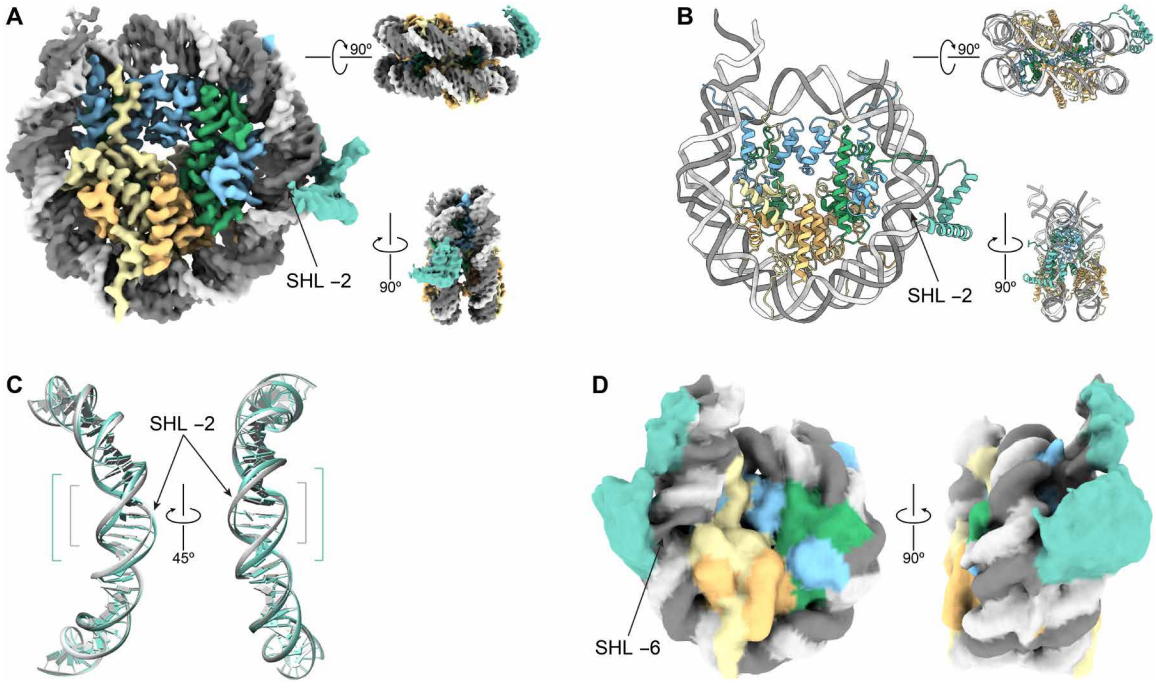

Fig. 2. HMGB1 distorts nucleosomal DNA at multiple sites. (**A**) Cryo-EM density map of the A box of HMGB1 bound to a 0/10 nucleosome at SHL −2 at 2.9-Å resolution. (**B**) Atomic model built using the density in (A). (**C**) A comparison of the DNA bound by HMBG1 at SHL −2 (gray) to the unbound DNA at SHL +2 (teal), showing the widening of the minor grove by the HMG box. (**D**) An additional cryo-EM class revealed by cryoDRGN showing extra density for HMGB1 bound at SHL −6.

SOX11 (*44*). However, unlike the SOX proteins, this structure of an ancestral HMG box protein shows binding to this site in a sequence-independent manner. The ability to bind an internal nucleosomal site such as SHL −2 may therefore more generally represent an intrinsic capability of HMG box domains.

While the local resolution of the HMG box density was insufficient for de novo model building, we find that the density most likely represents box A of HMGB1 by docking previously determined models of HMGB1 box A and box B [Protein Data Bank (PDB) 4QR9 and PDB 2GZK, respectively] (*47*, *48*) into the cryo-EM density followed by real space refinement (Fig. 2B and fig. S7). We base this interpretation on the ability to see density for phenylalanine in box A but not in box B (fig. S7) and the fact that box A bends DNA less than box B (*49*), which would make it more likely to fit the curvature of nucleosomal DNA. Similar to the structure of SOX2 bound nucleosomes, we see a 6-Å widening of the minor groove of the nucleosomal DNA at SHL −2 (Fig. 2C and fig. S8), consistent with the effect of HMG box domains on DNA. Because of HMGB1's high off rate, we could only resolve a single HMG box in our structure, while there could be up to four HMG boxes if two HMGB1 molecules are bound to a single nucleosome. We hypothesize that there are other regions of nucleosomal DNA where the HMG boxes can transiently interact that are being averaged out in our structure. Thus, there may be an ensemble of rapidly interconverting nucleosome bound conformations of HMGB1.

To visualize other conformations of HMGB1 on nucleosomes that may be present in our dataset, we used the cryoDRGN heterogeneity analysis (*50*). Although this analysis revealed that most of the particles in our dataset are relatively similar, based on the overlap of most nucleosomal classes on the Uniform Manifold Approximation and Projection plot (fig. S9A), it also identified various structural classes from within our dataset, including ones that correspond to HMGB1 bound at SHL −2 as detected by our earlier analysis (fig. S9B, volumes 3, 4, 5, and 13). In one particular class (fig. S9B, volume 16), there is extra density at SHL −6, which we interpret to be HMGB1 (Fig. 2D). In addition, in a related reconstruction, we also see a modest nucleosomal DNA kink at SHL −6 although HMGB1 density is more poorly resolved (figs. S9 and S10, volume 19). The DNA distortions at SHL −6 in these two classes are consistent with our REA results, where we see an increase in DNA accessibility at position 137, which resides between SHL −6 and −7. Together, these structures imply that the two HMG boxes of HMGB1 bind transiently at multiple sites along the nucleosomal DNA. These findings are inconsistent with the prevalent model of binding competition between HMGB1 and H1 as none of the observed HMGB1-binding sites overlap with H1's binding site at the dyad. In addition, in support of our results on core nucleosomes, we see that HMGB1 is able to directly interact with nucleosomal DNA at multiple sites. When we do observe binding of an HMG box, it correlates with modest local distortion of the nucleosomal DNA. Rapid binding and unbinding of the two HMG boxes and corresponding transient DNA distortion at multiple sites could contribute to HMGB1's overall effect of increasing nucleosomal DNA accessibility. Further, if the C terminus is anchored by the H3 tail, such positioning could synergize with preferential DNA unwrapping at the entry/exit sites, where DNA is less restricted by contacts with the octamer core.

HMGB1 and H1 directly obstruct each other's effects on nucleosomes

Previous biochemical studies have investigated the effects of either HMGB1 alone or H1 alone on nucleosomes, but no studies to date have investigated the biochemical effects of one protein in the

presence of the other. Therefore, to test how HMGB1 and H1 influence each other's activities, we performed REA experiments in the presence of both proteins on a minimal nucleosome substrate for H1 binding (10/10-Pst137) (*27*). Consistent with previous REA results using *Drosophila* H1 (*43*), when nucleosomes are bound by H1 there is no detectable cutting (Fig. 3A), as a closed conformation of the entry/exit DNA is stabilized by H1 (*51*). However, even when HMGB1 is added at concentrations 16-fold over its K_d for nucleosomes, cutting is not recovered (Fig. 3, A and B). H1's K_d for nucleosomes is in the picomolar-nanomolar range (*27*), compared to the micromolar K_d for HMGB1 (fig. S2C). The stronger affinity of H1 compared to HMGB1 suggests that equilibration of H1 binding to nucleosomes may take longer than that of HMGB1, potentially providing HMGB1 an advantage if the two proteins are added simultaneously. Consistent with this possibility, we found that when we added the two proteins simultaneously, HMGB1 can modestly rescue some detectable cutting (fig. S11). This suggests that the time taken for H1 to equilibrate on nucleosomes is slower than that of HMGB1 because of a combination of slow on and off rates of H1. Yet, overall HMBGB1 is not very effective in countering H1's

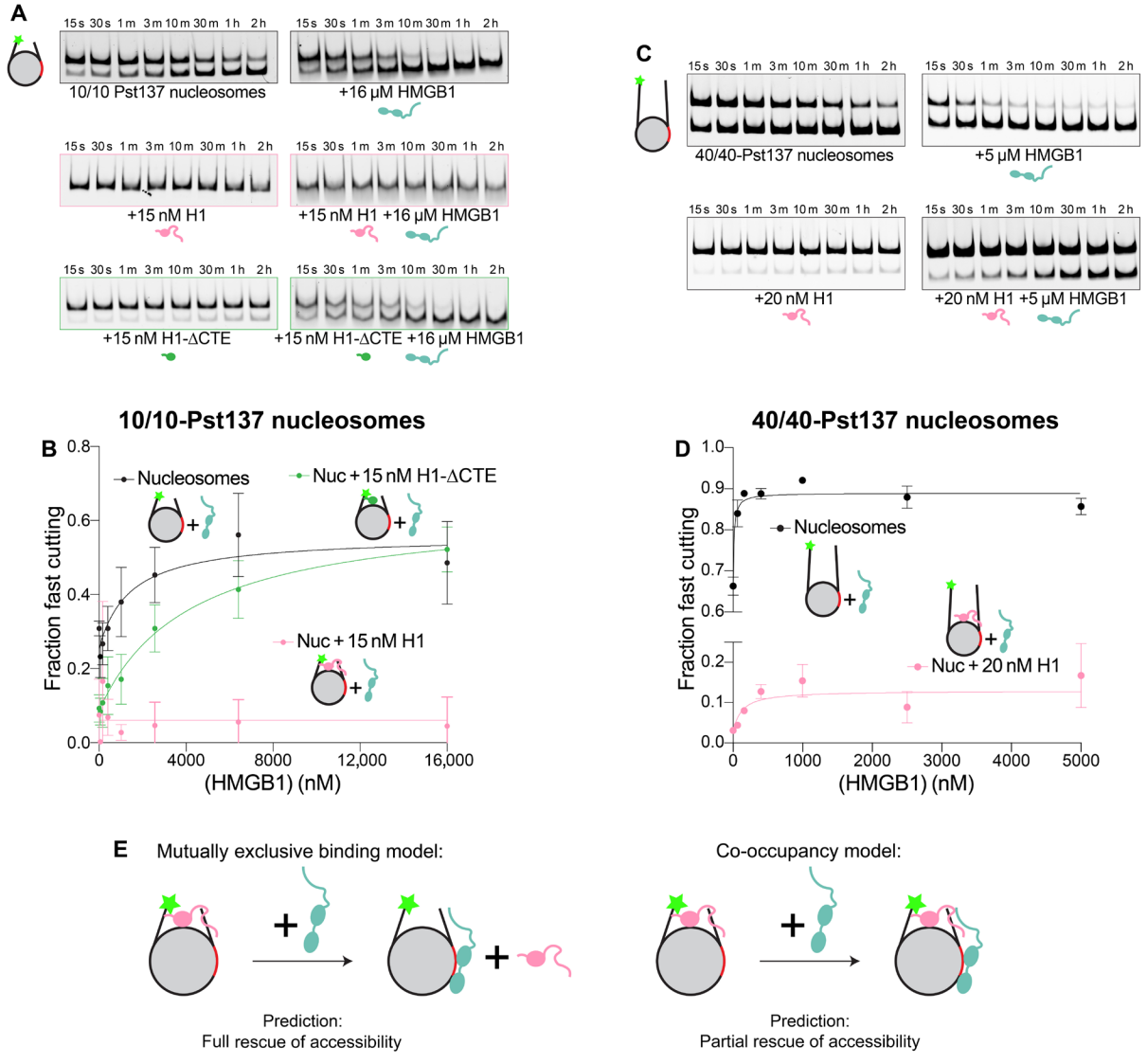

Fig. 3. HMGB1 and H1 compete to tune nucleosomal DNA accessibility. (**A**) Representative time-course gels of REA experiments in the presence of indicated concentrations of H1 and/or HMGB1. (**B**) The fraction of fast-cutting nucleosomes is shown as a function of HMGB1 concentration. Before HMGB1 is added, 10/10-Pst137 nucleosomes are either bound by no H1 (black), 15 nM H1 (coral), or 15 nM H1-ΔCTE (green). Curve represents a fit by the equation derived from the model in (Fig. 1G). (**C**) Representative REA time courses of 40/40-Pst137 nucleosomes with or without H1 and/or HMGB1. (**D**) The fraction of fast cutting nucleosomes is shown as a function of HMGB1 concentration. 40/40-Pst137 nucleosomes are either bound by no H1 (black) or 20 nM H1 (coral) before HMGB1 was added. Curve represents a fit by the equation derived from the model in (Fig. 1G). $K_{1/2}$ is 14.1 nM for nucleosomes alone and 112.6 nM for nucleosomes + H1. (**E**) A schematic of the predictions of the mutually exclusive binding model and the co-occupancy model. The mutually exclusive binding model would predict that saturating HMGB1 would displace H1 from nucleosomes, totally rescuing nucleosomal DNA accessibility. The co-occupancy model would predict that saturating HMGB1 would not displace H1 from nucleosomes and nucleosomal DNA accessibility would only be partially rescued, which is what is observed in (D).

activity on 10/10 nucleosomes. A large difference in affinities could in principle explain why HMGB1 may not displace H1. However, this explanation does not take into account that the two proteins can interact with each other via their oppositely charged C-terminal tails (*19*). We therefore hypothesized that this direct interaction enables H1's inhibition of HMGB1 activity on 10/10 nucleosomes. To test this possibility, we investigated the effects of a mutant of H1 (H1-ΔCTE), which lacks the C-terminal basic tail that interacts with HMGB1. This construct still inhibits DNA unwrapping in our REA assay (Fig. 3A). However, the inhibition of unwrapping is rescued by HMGB1 in a concentration-dependent manner (Fig. 3, A and B). One interpretation of this result is that direct interaction between the two proteins via their C-terminal tails is essential for H1's inhibition of HMGB1. However, deletion of H1's C-terminal tail is known to reduce its affinity for nucleosomes ~100-fold (*27*). Therefore, an alternative explanation is that due to the lower affinity of the H1-ΔCTE protein, HMGB1 can now compete for binding.

In mammalian chromatin, linker lengths vary from 5 bp to more than 100 bp (*52*). To investigate the HMGB1 and H1 interplay in the context of linker lengths longer than 10 bp, we used nucleosomes with 40 bp of flanking DNA on either side (40/40-Pst137). Similar to the 10/10 nucleosomes, H1 strongly inhibits REA on 40/40 nucleosomes (Fig. 3C). However, unlike 10/10 nucleosomes, on 40/40 nucleosomes, HMGB1 can partially rescue the inhibition of DNA unwrapping caused by H1, indicating that linker DNA length tunes the competition between HMGB1 and H1 (Fig. 3C). A competition model where binding of H1 and HMGB1 is mutually exclusive predicts that at some saturating concentration of HMGB1, H1 would be fully displaced from the nucleosome (Fig. 3E). At such a concentration, the nucleosomal DNA accessibility should match that observed when HMGB1 is added to nucleosomes in isolation (Fig. 3E). However, we observe that in the presence of higher concentrations of HMGB1, nucleosomal DNA accessibility saturates at an intermediate level between H1-inhibited and fully HMGB1-enhanced (Fig. 3, C and D). This result indicates that HMGB1 counteracts the effects of H1 without displacing H1 from nucleosomes and implies that HMGB1 and H1 can co-occupy a nucleosome. In addition, the concentration at which DNA unwrapping is 50% rescued ($K_{1/2}$) is 112.6 nM (Fig. 3D), similar to HMGB1's K_d for DNA and 40/40 nucleosomes (fig. S2C). This finding suggests that HMGB1 binding to 40/40 nucleosomes is insensitive to the presence of H1, further implying the formation of a ternary complex. Unlike on 10/10 nucleosomes, the flanking DNA on 40/40 nucleosomes is sufficient to accommodate an entire HMGB1 molecule. We therefore propose that 40/40 nucleosomes provide more HMGB1-binding sites on the flanking DNA, thereby changing how HMGB1 and H1 interact and compete.

To more directly test the possibility of a ternary complex of HMGB1 and H1 on nucleosomes, we developed a Förster resonance energy transfer (FRET) assay to monitor H1 binding to 40/40 and 10/10 nucleosomes (fig. S12). Upon addition of H1, we observe a quenching of the nucleosomal donor fluorescence and an increase in the H1 acceptor fluorescence (figs. S12, B, G, and L). Under the reaction conditions of our REA assay, when HMGB1 was added at saturating concentrations, H1 acceptor fluorescence was maintained on all nucleosomal substrates tested (fig. S12, D, E, I, J, L, and M). In addition, when HMGB1 is added to nucleosomes in the absence of H1, we observed quenching of the nucleosomal donor fluorophore, providing a means to directly assay HMGB1 binding to nucleosomes (fig. S12, C and H). In the presence of H1, this quenching effect was preserved while also maintaining the FRET with H1 (fig. S12, C and H), providing evidence that HMGB1 and H1 can form a ternary complex on a nucleosome.

HMGB1 stimulates nucleosomal DNA accessibility within chromatin fibers

We next asked whether HMGB1 promotes access to nucleosomal DNA in the context of a chromatin array template. To look at accessibility of DNA within chromatin, we used the single-molecule adenine methylated oligonucleosome sequencing assay to test chromatin accessibility on assembled templates (SAMOSA-ChAAT) (*53*). We assembled nucleosomes onto a DNA template containing 12 successive 601 sequences interspersed by 46 bp of flanking DNA (*54*). The pattern of DNA accessibility within the chromatin array showed increased and asymmetric accessibility near the entry/exit sites of the nucleosome (Fig. 4, A and B), consistent with intrinsic nucleosomal DNA unwrapping and the asymmetry of the 601 sequence (*3*, *55*). With increasing HMGB1 concentrations, the nucleosomal DNA within the chromatin arrays became more exposed (Fig. 4A). Furthermore, we see that the increase in DNA accessibility is most pronounced near the entry/exit sites of the nucleosome resulting in a decreased nucleosome footprint size (Fig. 4, B and C), consistent with the model that HMGB1 enhances existing unwrapping dynamics to expose nucleosomal DNA. The increase in restriction enzyme cutting we observe at position 137 with nucleosomes is well within the region of increased accessibility we observe by SAMOSA-ChAAT on chromatin arrays, suggesting that HMGB1 acts similarly on nucleosomes within chromatin arrays as it does on mononucleosomes.

At the highest concentration of HMGB1 tested, we notice a decrease in accessibility and a larger footprint (12.5 μM HMGB1; Fig. 4, A to C). We attribute this effect to bending of the linker DNA caused by binding of additional HMGB1 molecules leading to internucleosome interactions that inhibit access to nucleosomal DNA. This possibility is consistent with previous observations showing that yeast Hmo1 and Nhp6 can promote compaction of chromatin arrays (*42*).

To explore how HMGB1 and H1 compete to regulate DNA accessibility within chromatin, we performed SAMOSA-ChAAT on chromatin arrays in the presence of both proteins. Previous studies have shown that binding of linker histone decreases accessibility of the linker DNA resulting a larger, "chromatosome" footprint (*15*, *32*, *51*, *56*). Consistent with these studies, when we add H1 to our arrays, the amount of DNA protection increases (Fig. 4D). When increasing amounts of HMGB1 are added in the presence of H1, we see a corresponding rescue of DNA accessibility notably within the flanking DNA (Fig. 4D), which would have been invisible in our REA assay. Consistent with our REA results, HMGB1 also rescues the accessibility of nucleosomal DNA within arrays, evidenced by a decrease in the average nucleosome footprint size at higher HMGB1 concentrations (Fig. 4, E and F). Overall, these findings indicate that the opposing effects of HMGB1 and H1 observed on mononucleosomes translate to a chromatin substrate.

HMGB1 makes H1 and condensed chromatin more dynamic

Chromatin arrays also provide the opportunity to test the dynamics of HMGB1 and H1 in the context of condensed chromatin, which may more accurately recapitulate in vivo chromatin properties. Cellular

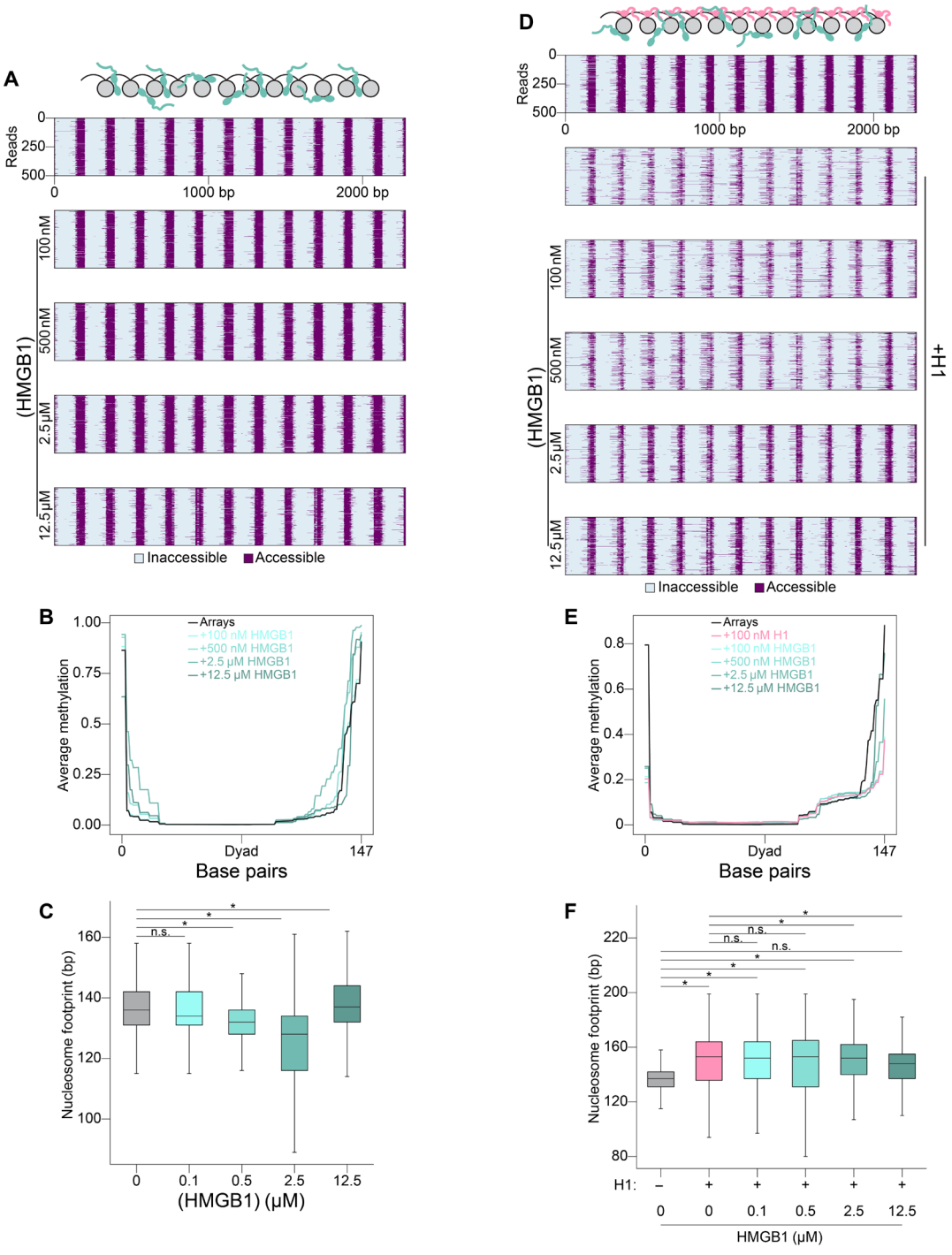

Fig. 4. HMGB1 increases accessibility of DNA within chromatin. (**A**) Heatmaps of SAMOSA-ChAAT experiments showing nucleosome footprints on a 12-by-601 array with a range of HMGB1 concentrations. Purple represents DNA that is accessible as assessed by the presence of adenine methylation. Gray represents DNA that is inaccessible as assessed by the lack of methylation and is interpreted as a nucleosome footprint. (**B**) The average methylation across every 601 sequence within the array is combined to show an average nucleosome footprint within the array. (**C**) Box and whiskers plot of nucleosome footprint size as a function of HMGB1 concentration. Solid line represents the median footprint size, while the height of the box represents the interquartile range, and the error bars represent the farthest data point within 1.5× the interquartile range from the box. Asterisks represent a *P* value < 0.01 on a two-tailed *t* test. n.s., not significant. (**D**) Heatmaps of SAMOSA-ChAAT experiments showing nucleosome footprints on a 12-by-601 array with H1 and a range of HMGB1 concentrations. Purple and gray represent accessible and inaccessible DNA, respectively as in (A). (**E**) The average methylation across every 601 sequence within the array is combined to show an average nucleosome footprint within the array. (**F**) Box and whiskers plot of nucleosome footprint size as a function of HMGB1 concentration. Solid line represents the median footprint size, while the height of the box represents the interquartile range, and the error bars represent the farthest data point within 1.5× the interquartile range from the box. Asterisks represent a *P* value <0.01 on a two-tailed *t* test. n.s., not significant.

data on the competition between HMGB1 and H1 come from fluorescence recovery after photobleaching (FRAP) studies, which showed that fluorescently labeled H1 recovers faster in the presence of increased concentrations of HMGB1 (*16*). However, it is unclear whether this effect is due to direct binding competition between HMGB1 and H1 or some indirect effect. To investigate any direct effects of HMGB1 on H1's binding and turnover dynamics within condensed chromatin, we used well-established previous methods to generate phase-separated chromatin condensates in vitro (*54*). We compacted the chromatin arrays by the addition of 3 mM $MgCl_2$ and 100 mM KCl in the presence or absence of Alexa Fluor 555–labeled H1 such that H1 to nucleosome stoichiometry is 1:1 and varied the concentration of HMGB1. HMGB1 causes chromatin condensates containing H1 to become larger, although we see no loss of H1 intensity within condensates (Fig. 5, A and B). These results suggest that even in condensed chromatin, HMGB1 does not simply displace H1 and are consistent with our data suggesting co-occupancy of HMGB1 and H1 on nucleosomes. We next explored whether HMGB1 affects the dynamics of H1 within condensed chromatin as has been reported in vivo (*16*).

Consistent with previous results (*54*), we observe that in the absence of HMGB1, H1 fluorescence recovers to about 45% of prebleach intensity within 2 min (Fig. 5C). Upon addition of HMGB1, we observe an increase in the rate of recovery and the mobile fraction of H1 that recovers, both of which are HMGB1 concentration–dependent (Fig. 5, C to E). Together with the observation that HMGB1 does not decrease the amount of H1 in condensates, we conclude that HMGB1 alters the on/off dynamics of H1's interaction with chromatin but that binding of HMGB1 and H1 to chromatin is not mutually exclusive.

This finding raises the possibility that while HMGB1 and H1 do not compete by binding the same site within chromatin, their activities on regulating chromatin dynamics are in competition with one another. To investigate this possibility, we performed FRAP on the Alexa Fluor 647–labeled chromatin arrays within condensates. Consistent with previous FRAP results within chromatin condensates (*54*), we find that 70% of the chromatin recovers to prebleach intensity within 5 min (Fig. 5F). The addition of H1 slows recovery by ~threefold and reduces the fraction that recovers to 25%, also consistent with previous results (Fig. 5, F to H) (*54*). Upon addition of increasing amounts of HMGB1, we see a partial rescue of chromatin dynamics (Fig. 5F). HMGB1 restores the mobile fraction of chromatin to 60% but does not increase the rate constant of recovery (Fig. 5, G and H). This result suggests that HMGB1's effect is due to altering H1's activity since in the absence of H1, HMGB1 has minimal effect on chromatin dynamics (fig. S13). Together with results showing that H1 is not displaced from the condensates, these findings provide further evidence that HMGB1 and H1 modulate each other's activities while co-occupying chromatin.

DISCUSSION

Compared to its competitor H1, less is known about HMGB1's interaction with nucleosomes and its effects on chromatin at the mesoscale. Our findings suggest that HMGB1 enhances the dynamics of nucleosomes through rapid sampling and local distortion of multiple locations on nucleosomal DNA by its HMG boxes while its C terminus is anchored by the H3 tail. Our results also shed light on the competition between HMGB1 and H1. Whereas H1 inhibits dynamics of nucleosomes and chromatin, HMGB1 appears to act as a molecular stir bar to increase chromatin dynamics at multiple scales. This interplay between these two abundant nuclear architectural proteins presents additional opportunities for chromatin regulation. Below, we discuss the mechanistic and biological implications of our findings in the context of previous results.

Multiple modes of engagement explain how HMGB1 enhances nucleosome dynamics

Substantial previous work has led to the model that HMGB1 exposes nucleosomal DNA through its DNA bending activity (*21*, *40*, *41*, *57*–*60*). Work with the H3 tail peptide indicates that interactions between the C-terminal tail of HMGB1 and the H3 tail relieve autoinhibition to enhance DNA binding of the HMG boxes (*39*). Here, we have directly tested these models in the context of a nucleosome. Our results show that the HMG boxes interact with and locally deform nucleosomal DNA. Further, our results suggest an additional role for the interaction between HMGB1's C-terminal tail and the H3 tail. Not only does this interaction sequester the H3 tail away from nucleosomal DNA, allowing DNA to unwrap more readily and relieve autoinhibition of the HMG boxes as proposed previously (*39*), but our results also imply that the H3 tail also orients HMGB1 on nucleosomes in a way that promotes unwrapping of nucleosomal DNA (Fig. 6A). We propose that interaction of the C-terminal tail of HMGB1 with the H3 tail spatially localizes the HMG boxes to certain regions of nucleosomal DNA, such as SHL −2 and SHL −6. Among these sites, those where nucleosomal DNA is less restricted by histone interactions, HMG box-induced DNA bending is more likely to result in unwrapping. How HMGB1's specificity for the H3 tail is encoded by the low complexity, Asp/Glu-rich C-terminal tail remains an open question. One possibility is that the proximity of the H3 tail near the entry/exit DNA places it near preferred HMGB1-binding sites on flanking DNA, SHL −2 or SHL −6. Another possibility is that the longer length of the H3 tail provides a larger interaction surface for the HMGB1 C-terminal tail resulting in a stronger interaction compared to the other, shorter histone tails.

Further, we speculate that HMGB1's high off rate and the dynamic interconversion between bound and unbound states allow the nucleosome to rapidly sample multiple states in which different regions of nucleosomal DNA become accessible. In such a model, HMGB1 increases the number of nucleosomal conformational states in the system while lowering the activation barrier between these states. Substantial previous work has uncovered how histone chaperones catalyze interconversions between assembled and disassembled nucleosomes and how ATP-dependent chromatin remodelers slide and conformationally alter nucleosomes (*2*, *61*). This mechanism for HMGB1 provides a third and qualitatively distinct way to make nucleosomal DNA accessible by promoting a rapid equilibrium between differently bound states, each with a different region of nucleosomal DNA made more accessible.

HMGB1 and H1 oppose one another's activities as a function of flanking DNA length

Our data suggest that HMGB1 and H1 counteract each other's activities while co-occupying a nucleosome. Further, the ability of HMGB1 to counteract H1's inhibition of DNA unwrapping increases with increasing flanking DNA length or when the H1 C-terminal tail is deleted. H1 reduces nucleosome dynamics by interacting with and stabilizing the flanking DNA proximal to the entry/exit site

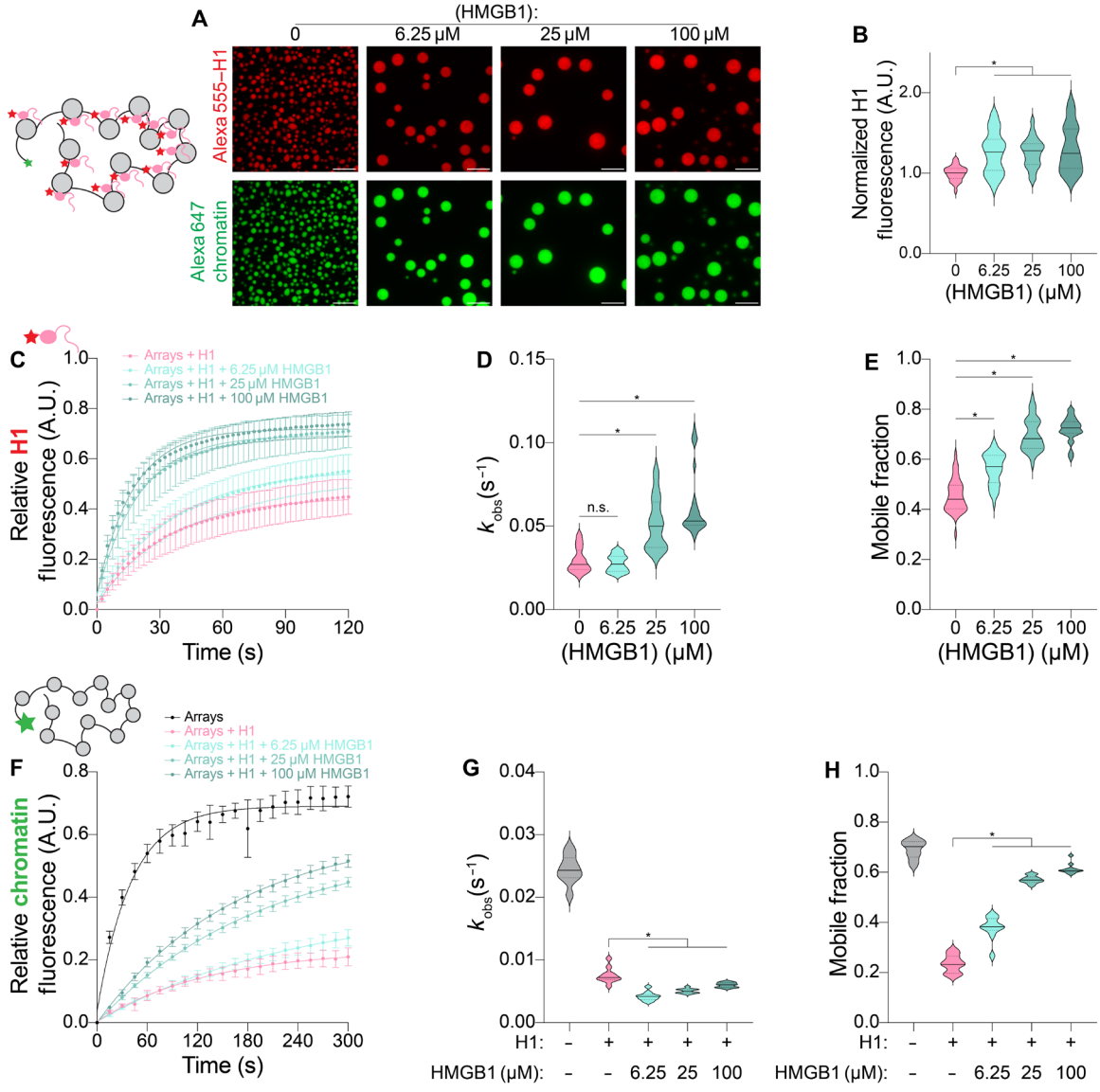

Fig. 5. HMGB1 increases the turnover dynamics of H1 and chromatin. (**A**) Representative microscopy images of chromatin condensates. Thirty nanomolar Alexa Fluor 647–12-by-601 arrays are mixed with 360 nM Alexa Fluor 555–H1 and varying concentrations of HMGB1. Scale bar, 10 μm. (**B**) Violin plots of the quantification of the average Alexa Fluor 555–H1 fluorescence intensity within chromatin condensates. All values are normalized to chromatin and H1 alone with no HMGB1 added. Solid and dotted lines represent the median and interquartile values, respectively. Values represent an average of three experimental replicates with $n > 10$ condensates per replicate. Asterisks represent a P value < 0.01 on a two-tailed t test. (**C**) Quantification of the FRAP of Alexa Fluor 555–H1 within chromatin condensates. Values are normalized from 0 to 1 corresponding to post and prebleach, respectively. Points represent an average of three experimental replicates with $n > 10$ condensates per replicate. Error bars represent SD of all condensates within the three replicates. Data are fit to a one-phase exponentially association. (**D** to **E**) Violin plots of the quantification of the fits to the FRAP data in (C). The rate constant for recovery (k_{obs}) and the plateau of recovery (Mobile Fraction) are plotted for the four different conditions in [(D) and (E)], respectively. Solid and dotted lines represent the median and interquartile values, respectively. Asterisks represent a P value < 0.01 on a two-tailed t test. (**F**) Quantification of the FRAP of Alexa Fluor 647–12-by-601 arrays within condensates. Values are normalized from 0 to 1 corresponding to post and prebleach, respectively. Points represent a single experimental replicate with $n > 10$ condensates. Error bars represent SD of all condensates. Data are fit to a one-phase exponentially association. (**G** and **H**) Violin plots of the quantification of the fits to the FRAP data in (F). The rate constant for recovery (k_{obs}) and the plateau of recovery (Mobile Fraction) are plotted for the five different conditions in [(G) and (H)], respectively. Solid and dotted lines represent the median and interquartile values, respectively. Asterisks represent a P value < 0.01 on a two-tailed t test.

(*51*). It is also proposed that interaction between the HMGB1 C-terminal tail and the H1 C-terminal tail relieves autoinhibition of HMGB1 (*19*). We hypothesize that on nucleosomes with short flanking DNA (10 bp or less), HMGB1 can interact with the H1 C-terminal tail but that this interaction does not sufficiently outcompete the interaction of the H1 tail with nucleosomal DNA. As a result, on nucleosomes with 10 bp of flanking DNA, HMGB1 cannot overcome H1's inhibition of DNA unwrapping. However, when longer-flanking DNA is present, the H1 C-terminal tail can now bind flanking DNA as well as nucleosomal DNA and additional HMGB1 molecules can be accommodated on the flanking DNA in addition to the core nucleosome (Fig. 6B). We propose that in this context,

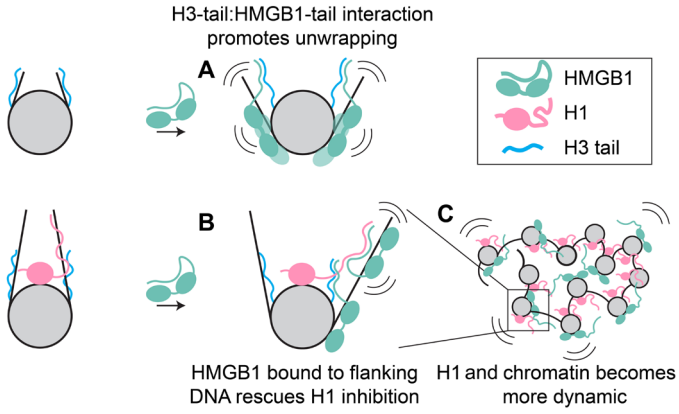

Fig. 6. HMGB1 and H1 compete to regulate chromatin dynamics across scales. (**A**) HMGB1 promotes unwrapping through interaction with the H3 tail. This replaces the H3 tail's interaction with nucleosomal DNA and relieves autoinhibition of HMGB1, allowing the HMG boxes to bind and deform nucleosomal DNA. (**B**) When longer flanking DNA is present, HMGB1 is able to rescue H1 inhibition of DNA unwrapping. The extra flanking DNA allows additional HMGB1 molecules to interact, which loosens H1's interaction with the flanking DNA, allowing HMGB1 to rescue DNA unwrapping. (**C**) HMGB1's loosening of H1's interaction with flanking DNA makes both H1 and chromatin itself more dynamic within condensed chromatin.

the C-terminal tails of HMGB1 and H1 interact, resulting in (i) stabilization of HMG box binding to flanking DNA, (ii) displacement of the H1 tail from flanking DNA, and (iii) bending of the flanking DNA by the HMG box. In addition, the bending of flanking DNA by HMGB1 binding could enable additional HMGB1 molecules to more readily bind and distort nucleosomal DNA at locations such as SHL −2. Together, these coupled outcomes would increase the probability of DNA unwrapping. In this model, HMGB1's interaction with the H1 C-terminal tail on flanking DNA is key to tuning the two proteins' effects on DNA accessibility.

Deletion of H1's C-terminal tail increases H1's turnover in vivo and in vitro (*24*, *54*). We find that HMGB1 increases H1's turnover dynamics within condensed chromatin in vitro, consistent with the model that the interaction between HMGB1 and H1's C-terminal tail loosens the H1 C-terminal tail's interaction with nucleosomal and flanking DNA. This HMGB1-H1 interaction would also rescue H1's inhibition of chromatin dynamics since the H1 C-terminal tail is necessary for its inhibition of chromatin turnover (*54*). In this way, addition of HMGB1 to H1 chromatin makes H1 behave more like H1-ΔCTE. We observe only minor effects of HMGB1 on chromatin dynamics in the absence of H1, emphasizing the importance of the HMGB1-H1 tail-tail interaction in HMGB1's ability to rescue H1's inhibition of chromatin dynamics.

The dynamics of chromatin at the mesoscale are regulated by the lifetimes of interactions between nucleosome arrays, which are in turn mediated by internucleosomal interactions. Previous FRAP studies have implied that interarray interactions are enhanced in the presence of linker histone and by interactions between histone tails and nucleosomal DNA (*54*). We propose that the H1 C-terminal tail's interaction with flanking DNA stabilizes low-energy and long-lived internucleosomal interactions between arrays, which promote condensation of chromatin but reduce chromatin dynamics. HMGB1 enhances dynamics in part by weakening H1's affinity for flanking DNA, hindering H1's ability to stabilize these low-energy states. HMGB1 also sequesters the H3 tail, which increases DNA unwrapping dynamics. We propose that both of these effects disrupt conformations with long-lived internucleosomal contacts and result in new, high-energy internucleosomal interactions facilitated by the weak, transient interactions among HMGB1, H3, H1, and DNA. The lowered energetic barrier for switching between these different states could result in shorter-lived internucleosomal interactions and more rapid turnover of chromatin at the mesoscale (fig. S15). Overall, by creating more high-energy conformational states of chromatin, HMGB1 may function as a molecular stir bar, enhancing the dynamics of nucleosomes and condensed chromatin.

Mechanistic basis for HMGB1's diverse roles in vivo

Overexpression of HMGB1 has been linked to transcription activation (*12*), suggesting that HMGB1 reduces the inhibitory effect of nucleosomes. A knockout of HMGB1 in mouse cells is associated with a global reduction of nucleosomes, and in vitro, HMGB1 enhances the assembly of chromatin (*62*–*64*). Our findings provide a molecular explanation for these results. We observe that HMGB1 drives a transient increase in nucleosomal DNA accessibility and distorts nucleosomal DNA without disassembling the nucleosome. We therefore propose that HMGB1-induced nucleosomal DNA flexibility allows nucleosomes to dynamically accommodate transient structural changes in DNA without falling apart. Such accommodation would increase nucleosome stability in the face of factors that try to access nucleosomal DNA. The FACT nucleosome chaperone complex, which protects nucleosomes from polymerases, contains an HMG box domain (*61*).

Consistent with the proposed model, HMGB1 has been shown to enhance the affinity of the estrogen receptor to a nucleosomal site and enhance ATP-dependent nucleosome remodeling by ISWI and SWI/SNF family of chromatin remodelers (*21*, *58*–*60*, *65*). HMGB1 has also been shown to increase binding of various TF's to DNA via DNA bending and direct interactions with the TF (*66*–*73*). We therefore speculate that a transient HMGB1-TF complex could act as a bipartite pioneer factor, enabling access to nucleosomal DNA sequences without disassembly of the histone octamer. The SOX family of pioneer factors contains HMG boxes that have evolved sequence specificity, hinting at a possible universal mechanism of HMG box domains for accessing nucleosomal DNA.

Our findings further suggest that the H3 tail-HMGB1 interaction not only releases autoinhibition by the HMGB1 C-terminal tail but also orients the HMG boxes for effective DNA unwrapping. Posttranslation modifications of the H3 tail could thus alter how HMGB1 interacts with nucleosomes and its effect on DNA accessibility and serve as a cue to where in the genome HMGB1 acts. One possibility is that HMGB1 cooperates with histone acetyltransferases to induce DNA accessibility. Consistent with this model, HMGB1 localizes to sites in the genome marked by acetylation of Lys^{27} on H3 (*74*).

Consequences of competition between HMGB1 and H1 in vivo

In vivo, HMGB1 and H1 have been shown to compete with one another despite HMGB1's lower concentration and weaker affinity to chromatin (*10*, *16*, *21*, *22*, *26*, *27*). Our model reconciles this paradox by providing a molecular mechanism whereby HMGB1 counteracts H1 activity without displacing it from chromatin. In this model, HMGB1 concentrations do not need to be high enough to competitively displace H1 from a nucleosome. HMGB1 concentrations

only have to be high enough to co-occupy nucleosomes in a manner that allows the C-terminal tail of HMGB1 to interact with the H1 tail. This model explains why in stem cells, where HMGB1 expression is highest, H1 turnover is increased compared to differentiated cells that have less HMGB1 (*17*, *18*), suggesting that HMGB1 may be especially important for pluripotency. HMGB1 expression is also elevated in some cancers, which could present an opportunity for therapeutic intervention (*18*).

Along with expression levels, phosphorylation of the H1 C-terminal tail could modulate the competition between HMGB1 and H1. In metaphase, when H1 phosphorylation is higher, HMGB1 is displaced from chromosomes while H1 remains bound (*23*, *75*). H1 phosphorylation has also been linked to both activation and repression of transcription (*76*–*78*), suggesting that there could exist a variety of modes of regulation of this competition via H1 phosphorylation. Further exploration of the role of H1 tail phosphorylation will reveal how competition with HMGB1 is modulated in vivo.

Recent attempts to determine nucleosome structures in situ have found that most nucleosomes do not have stable flanking DNA conformations, and many nucleosomes appear partially unwrapped (*79*–*83*). We propose that the competition between HMGB1 and H1 is responsible for creating some of these more heterogeneous nucleosome structures, yet HMGB1, due to its high off rate and multiple modes of binding cannot be captured structurally, unlike H1. Additional heterogeneity may also arise from variations in linker lengths as we find that flanking DNA length is an important factor that tunes the competition between HMGB1 and H1, with H1 effects predominating at shorter linker lengths and HMGB1 effects at longer lengths. Linker DNA lengths in vivo vary from 5 bp to more than 100 bp (*52*) and thus likely regulate where in the genome HMGB1 or H1 affect nucleosomal DNA accessibility.

This study emphasizes the essential role of architectural proteins in modulating global effects on chromatin dynamics. Despite what the name suggests, we find that the abundant architectural protein HMBG1 does not serve as a structural support for chromatin, but rather our data suggests that HMBG1 increases the dynamics and accessibility of chromatin to enable DNA access without nucleosome disassembly. Further, we propose that the interplay between HMGB1 and architectural proteins like H1 that act more canonically to inhibit chromatin dynamics increases the number of states of the system allowing chromatin dynamics to be finely tuned at the molecular and mesoscale.

MATERIALS AND METHODS

Preparation of DNA substrates

DNA used for mononucleosomes was generated using large-scale polymerase chain reaction (PCR) of a plasmid containing the Widom 601 sequence. Various primers, labeled with either Alexa Fluor 488, fluorescein, or Cy5 (IDT), were used to generate different lengths of flanking DNA around the 601 sequence. When noted in the text, the 601 sequence contained a restriction enzyme site for PstI at position 137. PCR products were run over an 8% acrylamide gel, and the band was cut out on the basis of the DNA ultraviolet shadow. The gel band was crushed by passage through a 5-ml syringe and soaked in 1× Tris-EDTA (TE) buffer overnight before the crushed gel was removed with a 0.22-μm filter. The DNA was further ethanol precipitated and resuspended in 1× TE.

DNA for chromatin arrays was generated from a plasmid containing 12 successive 601 sequences, interspersed by 46 bp of linker DNA (*54*). The plasmid was grown in STBL2 cells (Thermo Fisher Scientific) and giga prepped (QIAGEN). The plasmid was then digested with EcoRV to cut out the array sequence and digest the plasmid backbone. To make Alexa Fluor 647–labeled arrays for condensate experiments, the DNA was additionally digested with XhoI to leave a sticky end on one end of the DNA. The array DNA was then purified over a Sephacryl S-1000 column and fractions containing the array DNA were pooled and isopropanol precipitated, before being resuspended in 1× TE. We note that two successive runs over the S-1000 column were necessary to fully remove the plasmid backbone.

To generate labeled array DNA, the sticky end generated by XhoI digest was filled in using Klenow polymerase (Invitrogen) with an Alexa Fluor 647–labeled dCTP (Invitrogen) along with unlabeled dATP, dTTP, and dGTP according to the manufacturer's instructions. DNA was then purified by phenol:chloroform extraction and ethanol precipitation before resuspension in 1× TE.

Assembly of nucleosomes and chromatin arrays

Recombinant *Xenopus laevis* histones H3, H4, H2A, and H2B were expressed and purified from *Escherichia coli* as previously described (*84*). Histone octamer and dimer was then reconstituted as previously described (*84*). Mononucleosome and chromatin arrays were assembled via salt gradient dialysis as previously described (*84*). Mononucleosomes were further purified over a glycerol gradient. All samples were quantified using a NanoDrop to measure the concentration of DNA within the sample.

HMGB1 purification

A codon-optimized gene block of *Homo sapiens* HMGB1 sequence was generated by Twist Biosciences and cloned into a pBH4 plasmid backbone. Briefly, the construct contains an N-terminal 6xHis tag followed by a Tobacco Etch Virus (TEV) protease cleavage site, which when cleaved leaves a Gly-Ser linker before the start Met of HMGB1. The plasmid was transformed into Rosetta (DE3) competent cells (Sigma-Aldrich) and grown in 2xYT (20 g of tryptone, 10 g of NaCl, and 10 g of yeast extract per 1 liter) supplemented with carbenicillin (50 μg/ml) and chloramphenicol (25 μg/ml) at 37°C. Once the cells have reached log phase [optical density (OD) = 0.5 to 0.6], expression was induced with 1 mM isopropyl-β-D-thiogalactopyranoside (IPTG) at 37°C for 4 hours. The cells were then pelleted by spinning at 5000*g* for 30 min at 4°C, and pellets were stored at −80°C.

The pellets were resuspended in lysis buffer with 2× protease inhibitor [20 mM Hepes-KOH (pH 7.5), 500 mM KCl, 10% glycerol, 7.5 mM imidazole, 2 mM β-mercaptoethanol (BME), 2 mM phenylmethylsulfonyl fluoride (PMSF), pepstatin A (2 μg/ml), leupeptin (6 μg/ml), and aprotinin (4 μg/ml)]. The cell suspension was homogenized with a Dounce homogenizer. Cells were lysed with an Emulsiflex at 15,000 psi for 15 min. Lysate was then clarified by centrifugation at 40,000*g* for 30 min at 4°C. The lysate was then incubated with TALON affinity resin (Takara, 1-ml bead volume/1-liter bacterial culture) for 1 hour at 4°C while nutating. The beads were then washed in batch two times with two bead volumes of lysis buffer with 1× protease inhibitor [20 mM HEPES-KOH pH 7.5, 500 mM KCl, 10% glycerol, 7.5 mM imidazole, 2 mM BME, 1 mM PMSF, pepstatin A (1 μg/ml), leupeptin (3 μg/ml), and aprotinin (2 μg/

ml)] to remove any remaining lysate. Beads were then added to plastic disposable gravity columns and washed with 20 bead volumes of lysis buffer [20 mM Hepes-KOH (pH 7.5), 500 mM KCl, 10% glycerol, 7.5 mM imidazole, and 2 mM BME]. His-tagged HMGB1 was then eluted with 5 bead volumes of elution buffer [20 mM Hepes-KOH (pH 7.5), 150 mM KCl, 400 mM imidazole, and 2 mM BME] (fig. S16A). Cleavage of the His tag was then induced with TEV protease (150 μg of TEV/1 liter of bacterial culture) and left to dialyze overnight in TEV dialysis buffer [20 mM Hepes-KOH, 150 mM KCl, and 2 mM dithiothreitol (DTT)] (fig. S16B).

TEV-cleaved, full-length HMGB1 was then added to a Mono-Q anion exchange column equilibrated with 10% buffer QB [buffer QA: 20 mM Hepes-KOH (pH 7.5) and 3 mM DTT; buffer QB: 20 mM Hepes-KOH (pH 7.5), 1.5 M KCl, and 3 mM DTT]. HMGB1 was eluted from the Mono-Q column with a linear gradient from 10 to 60% buffer QB (150 to 900 mM KCl) over 20 column volumes. Full-length HMGB1 comes off between 32 and 35% buffer QB (~500 mM KCl), while many products that do not contain the full C-terminal tail come off at lower (KCl); therefore, this anion exchange step is crucial to obtaining pure, full-length HMGB1 (fig. S16, C and D). These fractions are then pooled and concentrated in a 3000-Da molecular weight cut off spin filter device. HMGB1 is finally purified over a Superdex 75 Increase size exclusion column equilibrated in size exclusion buffer [20 mM Hepes-KOH (pH 7.5), 300 mM KCl, 10% glycerol, and 3 mM DTT] (fig. S16, E and F). Fractions containing HMGB1 are pooled and concentrated in a 3000-Da molecular weight cut off spin filter device before being aliquoted, flash-frozen, and stored at −80°C in size exclusion buffer.

HMGB1-ΔC is purified identically, except a HiTrap SP cation exchange column is used in place of the Mono-Q anion exchange column, as the pI of HMGB1-ΔC is basic, while HMGB1-WT is acidic. A 10 to 60% gradient of buffer QB (150 to 900 mM KCl) is still used, and HMGB1-ΔC elutes between 29 and 33% buffer QB (~465 mM KCl). We do not see any contaminating expression products because the C-terminal domain has been removed.

H1 purification

H. sapiens H1.4 purification was adapted from (*54*) using a construct containing an N-terminal maltose-binding protein (MBP), followed by a TEV cleavage site, followed by H1.4 (full length or ΔCTE), followed by an additional TEV cleavage site, and then a C-terminal 6× His tag. This construct was transformed into Rosetta pLysS competent cells (EMD Millipore) and grown in 2xYT (20 g of tryptone, 10 g of NaCl, and 10 g of yeast extract per 1 liter) supplemented with carbenicillin (50 μg/ml) and chloramphenicol (25 μg/ml) at 37°C. Once the cells have just reached log phase (OD = 0.4), the cultures are moved to 18°C for 1 hour. After 1 hour, expression is induced with 0.5 mM IPTG for 18 hours at 18°C. Cultures are then pelleted at 5000*g* for 30 min at 4°C, and pellets are stored at −80°C.

Pellets are resuspended in lysis buffer with 2× protease inhibitor [20 mM Hepes-KOH (pH 7.5), 1 M NaCl, 10% glycerol, 7.5 mM imidazole, 2 mM BME, 2 mM PMSF, pepstatin A (2 μg/ml), leupeptin (6 μg/ml), and aprotinin (4 μg/ml)] The cell suspension was homogenized with a Dounce homogenizer. The cells were lysed with an Emulsiflex at 15,000 psi for 15 min. The lysate was then clarified by centrifugation at 40,000*g* for 30 min at 4°C. The lysate was then incubated with TALON affinity resin (Takara, 1.5 ml of bead volume/1 liter of bacterial culture) for 1 hour at 4°C while nutating. The beads were then washed in batch two times with two bead volumes of lysis buffer with 1× protease inhibitor [20 mM Hepes-KOH (pH 7.5), 1 M NaCl, 10% glycerol, 7.5 mM imidazole, 2 mM BME, 1 mM PMSF, pepstatin A (1 μg/ml), leupeptin (3 μg/ml), and aprotinin (3 μg/ml)] to remove any remaining lysate. Beads were then added to plastic disposable gravity columns and washed with 20 bead volumes of lysis buffer with 1× protease inhibitor [20 mM Hepes-KOH (pH 7.5), 1 M NaCl, 10% glycerol, 7.5 mM imidazole, 2 mM BME, 1 mM PMSF, pepstatin A (1 μg/ml), leupeptin (3 μg/ml), and aprotinin (2 μg/ml)]. Tagged H1 was then eluted with 5 bead volumes of elution buffer [20 mM Hepes-KOH (pH 7.5), 150 mM NaCl, 10% glycerol, 350 mM imidazole, 2 mM BME, 1 mM PMSF, pepstatin A (1 μg/ml), leupeptin (3 μg/ml), and aprotinin (2 μg/ml)]. Eluted protein was then incubated with amylose affinity resin (NEB, 2 ml of bead volume/1 liter of bacterial culture) for 1 hour at 4°C while nutating. The beads are then added to plastic disposable gravity columns and washed with 20 bead volumes of amylose wash buffer [20 mM Hepes-KOH (pH 7.5), 150 mM NaCl, 10% glycerol, 2 mM BME, 1 mM PMSF, pepstatin A (1 μg/ml), leupeptin (3 μg/ml), and aprotinin (2 μg/ml)]. H1 is then eluted with 5 bead volumes of amylose elution buffer [20 mM Hepes-KOH (pH 7.5), 150 mM NaCl, 10% glycerol, 2 mM BME, and 1% maltose]. Cleavage of the MBP and His tags was then induced with TEV protease (225 μg of TEV/1 liter of bacterial culture) and left to dialyze overnight in TEV dialysis buffer [20 mM Hepes-KOH, 150 mM KCl, and 2 mM DTT].

H1 is then loaded onto a HiTrap SP cation exchange column equilibrated with TEV dialysis buffer. H1 is then eluted with a linear gradient from 10 to 60% buffer SB [buffer SA: 20 mM Hepes-KOH (pH 7.5) and 2 mM BME; buffer SB: 20 mM Hepes-KOH (pH 7.5), 1.5 M NaCl, and 2 mM BME] over 20 column volumes. Fractions containing H1 were then incubated with 2 ml of bead volume of TALON affinity resin (Takara) for 1 hour at 4°C nutating to remove contaminating His-tagged TEV protease. The beads were removed using a plastic gravity column, and the flow through is concentrated using a 3000-Da molecular weight cut off spin filter device. H1 was then purified over a Superdex 75 Increase size exclusion column equilibrated in size exclusion buffer [20 mM Hepes-KOH (pH 7.5), 150 mM NaCl, 10% glycerol, and 1 mM DTT]. Fractions containing H1 were pooled and concentrated in a 3000-Da molecular weight cut off spin filter device before being aliquoted, flash-frozen, and stored at −80°C in size exclusion buffer.

For purification of fluorescently labeled H1, a Lys-Cys-Lys motif was added N-terminal to the start Met of H1. The protein was purified identically to H1-WT; however, before size exclusion chromatography, H1 was dialyzed overnight into labeling buffer [20 mM Hepes-KOH (pH 7.5), 150 mM NaCl, and 1 mM tris(2-carboxyethyl)phosphine (TCEP)]. Protein was then labeled with threefold molar excess of Alexa Fluor 555 maleimide (Invitrogen) at room temperature for 15 min. The labeling was quenched with 10-fold excess DTT. The protein was then concentrated using a 3000-Da molecular weight cut off spin filter device, and the unincorporated dye was removed by purification over a Superdex 75 Increase size exclusion column equilibrated in size exclusion buffer [20 mM Hepes-KOH (pH 7.5), 150 mM NaCl, 10% glycerol, and 1 mM DTT]. Fractions containing H1 were pooled and concentrated in a 3000-Da molecular weight cut off spin filter device before being aliquoted, flash-frozen, and stored at −80°C in size exclusion buffer.

REA assays

For all REA assays, 10 nM of fluorescently labeled nucleosomes containing a PstI site at position 137 within the nucleosomal DNA are used. Purified HMGB1 or H1 is added to nucleosomes in the presence of a 10× buffer that supplements to a final buffer of 19 mM Hepes-KOH (pH 7.5), 1 mM tris-HCl (pH 7.4), 30 mM KCl, 45 mM NaCl, 5 mM $MgCl_2$, 2 mM DTT, 9% glycerol, 0.11 mM EDTA, bovine serum albumin (BSA, 20 μg/ml), 0.015% Triton X-100, and 0.02% NP-40. Nucleosomes are allowed to equilibrate with HMGB1 or H1 for 30 min at 37°C. When both proteins are present, H1 is allowed to equilibrate first for 30 min before adding HMGB1 and waiting another 30 min to start the reaction, unless otherwise noted. The time course is started upon addition of PstI (NEB, 100 U/μl) to a final concentration of 10 U/μl. At each time point, 5 μl of the reaction is removed and added to a 2× REA Stop Mix [20 mM tris-HCl (pH 8), 70 mM EDTA, 2% SDS, and 20% glycerol). After the time course, 2 μl of proteinase K (NEB, 800 U/ml] is added to each time point and allowed to incubate for 30 min at 55°C. For reactions in which >5 μM of HMGB1 was added, an additional 2 μl of proteinase K (800 U/ml) was added after 15 min. After incubation, each time point is loaded onto a 8% acrylamide (29:1 acrylamide:bis) 1× tris/borate/EDTA (TBE) gel and run at 150 V for at least 2 hours. Gels are imaged using a Typhoon laser-scanning gel imager (GE). The fraction of DNA that is uncut is measured using ImageJ and plotted as a function of time. All nucleosome REA experiments are fit to a two-step exponential decay function in GraphPad Prism

$$\text{SpanFast} = (\text{Y0} - \text{Plateau}) \times \text{PercentFast} \times .01$$

$$\text{SpanSlow} = (\text{Y0} - \text{Plateau}) \times (100 - \text{PercentFast}) \times .01$$

$$\text{Y} = \text{Plateau} + \text{SpanFast} \times \exp(-\text{KFast} \times \text{X}) + \text{SpanSlow} \times \exp(-\text{KSlow} \times \text{X})$$

The fraction of nucleosomes that is cut fast is calculated using the following equation, which also factors in the fraction of nucleosomes that are not cut (Plateau)

$$\text{Fraction Fast} = \left[(1 - \text{Plateau}) \times \text{PercentFast}\right]/100$$

All REA experiments on DNA are fit to a one-step exponential decay function in GraphPad Prism

$$\text{Y} = (\text{Y0} - \text{Plateau}) \times \exp(-\text{K} \times \text{X}) + \text{Plateau}$$

Two-phase REA fitting and modeling

A model for how HMGB1 interacts with both fast and slow-cutting nucleosome populations is shown in Fig. 3E. The fraction fast calculated above is plotted as a function of HMGB1 concentration and fit to the following equations derived based on this thermodynamic cycle to calculate the K_d for the fraction that is cut fast and slow (K_d^f and K_d^s, respectively) and the overall half maximal concentration of HMGB1 ($K_{1/2}$)

$$Y = \left(K_{d^f} + X\right)/\left[\left(X/B_{max}\right) + \left(K_{d^f}/B_{min}\right)\right]$$

$$K_{d^s} = \left\{K_{d^f} \times \left[B_{max}/\left(1 - B_{max}\right)\right]\right\}/\left[B_{min}/\left(1 - B_{min}\right)\right]$$

$$\left(1/K_{1/2}\right) = B_{min}/K_{d^f} + \left(1 - B_{min}\right)/K_{d^s}$$

B_{min} and B_{max} represent the fraction of fast cutting nucleosomes when fully unbound (B_{min}) and fully bound (B_{max}).

Electrophoretic mobility shift assays

Fluorescently labeled nucleosomes (10 nM) were incubated with various concentrations of HMGB1 in the presence of a 10× buffer that supplements the final buffer composition to be 20 mM Hepes-KOH (pH 7.5), 75 mM KCl, 10% glycerol, 1 mM EDTA, 2 mM DTT, and 0.02% NP-40. Binding was allowed to equilibrate at room temperature for 30 min before loading onto a 6% acrylamide (29:1 acrylamide:bis) 0.5× TBE gel. The gel was run for 2.5 hours at 125 V and imaged using a Typhoon laser scanning gel imager (GE). The fraction of nucleosomes that are bound is calculated by measuring the unbound nucleosomes band and subtracting that value from the intensity of the whole lane. The fraction bound is then plotted as a function of HMGB1 concentration and fit to the following binding equation with the Hill coefficient N

$$Y = \left[\left(X\text{^N} \times B_{max}\right) + \left(K_d\text{^N} \times B_{min}\right)\right]/\left(X\text{^N} + K_d\text{^N}\right)$$

Cryo-EM sample preparation and data collection

HMGB1 and 0/10 nucleosomes were dialyzed separately into EM buffer [20 mM Hepes-KOH (pH 7.5), 25 mM KCl, 1 mM EDTA, 2 mM DTT, and 1.5% glycerol] overnight. Because of the relatively low affinity (micromolar range), HMGB1 was mixed with nucleosomes at final concentrations of 12 μM HMGB1 and 1 μM nucleosome and allowed to incubate at 20°C for 30 min before plunge freezing on Quantifoil R 1.2/1.3 200 mesh Au grids. Grids were cleaned beforehand for 15 s using a PELCO easiGLOW glow discharge system.

Sample grids were plunge frozen using an FEI Mark IV Vitrobot set at 4°C and 100% humidity. Three microliters of sample was applied to each grid. Each grid was blotted with humidity-saturated Whatman 1 filter papers for 3 s with a blot force of −1 before being plunge frozen into liquid ethane.

Sample grids were first screened using a 200 kV FEI Talos Arctica at UCSF. A larger dataset was then collected on two grids on a 300-kV Titan Krios at UCSF using a K3 camera at a nominal magnification of 105 kx (0.834 Å/pixels). All data were collected using Serial EM v3.7 or newer.

Cryo-EM data processing

Raw movies were motion-corrected using UCSF MotionCor2 v1.4.1 (*85*). Dose-weighted micrographs were imported into cryoSPARC v4.1.1 (*86*), and patch CTF estimation (multi) was used to estimate defocus values. Micrographs were filtered using Curate Exposures based on average defocus, estimated CTF, and relative ice thickness. A nucleosome map was used to generate templates for particle picking using Template Picker. A total of ~8.5 million particles were extracted at 288 pixel box downsampled to 72 pix. To remove junk particles, extracted particles were filtered through three rounds of Heterogeneous Refinement, where in each round a good nucleosome map and three junk maps (generated using Ab Initio on a small subset of remaining particles) were used as templates. After classification, the remaining good particles were reextracted at 288 pixel box downsampled to 192 pixels and duplicate picks were removed using Remove Duplicates, resulting in 561,888 particles.

The 561,888 particles were then used in Ab Initio to generate three classes, and the output volumes were used as templates for Heterogeneous Refinement to further classify the remaining particles. One good class containing 339,268 particles was further refined first using Homogenous Refinement and then Non-Uniform Refinement, optimizing for per-particle defocus and per-group CTF parameters. The resulting map showed a hint of density for an HMG box at SHL −2.

To further classify the particles for nucleosomes that contain an HMG box, the particles were exported using UCSF pyem v0.5 (*87*) to RELION v4.0 (*88*). 3D classification without alignment was performed using a spherical mask centered on the SHL −2 region. One class of four showed density for the HMG box domain, and the 47,813 particles in this class were imported back into cryoSPARC v4.1.1 and reextracted at 288 pixel box. One round of 2D classification was performed to remove the remaining obvious junk, resulting in 42,115 particles. This final set of particles was refined using Non-Uniform Refinement, resulting in the final map at ~3-Å global resolution for an HMGB1 box domain bound to nucleosome at SHL −2.

cryoDRGN analysis

The 339,268 particles that showed a hint of density for an HMG box at SHL −2 were reextracted at 300 pixels downsampled to 240 pixels. The particles were exported using UCSF pyem v0.5 to generate a .star file, and a corresponding .mrcs particle stack was generated using RELION. Inputs were preprocessed using cryoDRGN v1.1.2 (*50*) to generate pose and CTF .pkl files compatible with cryoDRGN. Images were downsampled further from 240 pixels to 120 pixels and used to train a cryoDRGN model with an 8D latent variable over 50 epochs of training. cryoDRGN analysis was then performed using the resulting model to visualize the latent space and generate density maps using default settings.

Model building

The ~3-Å global resolution output volume from cryoSPARC Non-Uniform Refinement was used to build a model for the HMGB1 box domain bound to nucleosome at SHL −2. The nucleosome from PDB 8V4Y (*89*) was used as the initial template for the nucleosome, and an HMGB1 Box A domain from PDB 4QR9 (*47*) was used as the initial template for the HMG box domain. DNA, histones, and the HMG box were adjusted using COOT v0.9.6 to account for differences in base pairs and residues that are resolved or not resolved in the current map. The ISOLDE plug-in (*90*) for UCSF ChimeraX v1.7.1 was used to correct for Ramachandran and rotamer outliers. COOT v0.9.6 was then used to correct bond angle and bond length outliers. The quality of all refined models was assessed using model validation in Phenix v1.18.2 and the wwPDB validation server.

FRET assay for H1-nucleosome binding

The donor fluorophore (either Alexa Fluor 488 for end labeled or fluorescein for internally labeled) was attached to the flanking DNA using labeled DNA and nucleosome assembly procedures described above. End-labeled 10/10 nucleosomes, end-labeled 40/40 nucleosomes, and internally labeled 40/40 nucleosomes were all used. For the internal label, the donor fluorophore was placed 20 bp in from the end of the DNA, so that it is in the middle of the flanking DNA once nucleosomes are assembled. N-terminally, Alexa Fluor 555–labeled H1 was used as the acceptor fluorophore. For FRET experiments, 10 nM of labeled nucleosomes were incubated first with 20 nM labeled H1 (or buffer) for 30 min at room temperature. Varying concentrations of HMGB1 (or buffer) were then added, and reactions were allowed to equilibrate for 30 min at room temperature. 10x buffer was supplemented such that the final buffer contained 20 mM Hepes-KOH (pH 7.5), 30 mM KCl, 45 mM NaCl, 5 mM $MgCl_2$, 0.1mM EDTA, 2 mM DTT, 4% glycerol, and 0.02% NP-40. Fluorescence spectra were read on an ISS K2 Multifrequency Phase Fluorometer. The donor fluorophore was excited at 470 nm with a short-pass filter at 550 nm. Emission spectra were then recorded from 500 to 600 nm. All samples were normalized to buffer blanks. FRET was calculated as the fluorescence intensity at 570 nm minus any interference of the donor emission at this wavelength using the following formula

$$\mathrm{FRET} = \mathrm{F}^{570\mathrm{nm}} - \mathrm{F}^{520\mathrm{nm}} \times X$$

The X value corrects for the interference of the donor fluorophore at 570 nm by calculating the ratio of fluorescence intensity at 570 and 520 nm in the absence of H1

$$X = \mathrm{F}^{570\mathrm{nm(noH1)}} / \mathrm{F}^{520\mathrm{nm(noH1)}}$$

X was calculated for each concentration of HMGB1 and each nucleosome construct to account for HMGB1's quenching effect of the donor fluorophore.

Single-molecule adenine methylated oligonucleosome sequencing assay to test chromatin accessibility on assembled templates

Unlabeled chromatin arrays (1 ng/μl) were incubated with varying concentrations of HMGB1 and H1 (50 nM when present) in the presence of 1× CutSmart Buffer (NEB), 2 mM DTT, and 1 mM *S*-adenosyl methionine in 100 μl. Binding was allowed to equilibrate for 30 min at 37°C. In the cases when HMGB1 and H1 were present, H1 was allowed to bind first for 30 min before addition of HMGB1 and an additional 30 min to equilibrate. To induce DNA methylation, 1 μl of EcoGII (NEB) was added to a final concentration of 50 U/ml. Methylation proceeded for 30 min at 37°C before adding 10 μl of 10% SDS and 2.5 μl of Proteinase K (NEB, 800 U/ml). Proteinase K digestion proceeded for 2 hours at 65°C. Methylated DNA was purified from these reactions via 1X SPRI Select Beads.

PacBio library preparation and sequencing

Entire binding reactions were used as input for PacBio SMRTbell library preparation. SMRTbell preparation of libraries was done using the SMRTbell prep kit 3.0 and included DNA damage repair, end repair, SMRTbell ligation, and exonuclease cleanup according to the manufacturer's instructions. After exonuclease cleanup and purification via 1x v/v SMRTbell cleanup beads, DNA concentration was measured by Qubit High Sensitivity DNA Assay (1 μl each sample). Data were collected over 30-hour Sequel II movie runs with 2 hours of preextension time and 2.1 polymerase.

SMRT data processing

Sequencing reads were processed as homogenous samples as described in (*53*) with slight variations.

Chromatin sample processing

Raw sequencing reads from chromatin samples were processed using software from Pacific Biosciences:

1) Generate CCS

Circular consensus sequences (CCSs) were generated for each sequencing cell using ccs 6.9.99. The --hifi-kinetics flag was used to

generate kinetics information (interpulse duration, or IPD) for each base of each consensus read. Values were stored for each base as 50 × (mean logIPD) + 1.

2) Demultiplex consensus reads

Consensus reads were demultiplexed using lima. The flag "–same" was passed as libraries were generated with the same barcode on both ends. This produces a BAM file for the consensus reads of each sample.

3) Align consensus reads to the reference genome

pbmm2, the pacbio wrapper for minimap2 (*91*), was run on each CCS BAM file (the output of step 2) to align reads to the reference sequence, producing a BAM file of aligned consensus reads.

Extracting interpulse duration measurements

The IPD values were accessed from the aligned, demultiplexed consensus BAM files.

Model training

Neural network, SMM, and SVD models were trained on fully methylated and unmethylated controls similarly to (*53*) but using IPD values from the aligned, demultiplexed consensus BAM files. The hidden Markov model was structured similarly to (*53*) but was refactored from pomegranate to use cython and numba.

Processed data analysis

All processed data analyses and associated scripts are available at GitHub. All analyses were computed using python. Plots were constructed via Matplotlib. Each analysis is briefly described below.

Defining inaccessible regions and counting nucleosomes

Inaccessible regions were called from HMM output data identically to (*52*). Briefly, inaccessible regions were defined as continuous stretches with accessibility ≤0.5. Periodic peaks were observed that approximated sizes of regions containing one, two, three, or more nucleosomes. Cutoffs for each size were manually defined using the histogram of inaccessible region lengths from a control sample.

FRAP of chromatin condensates

Purified HMGB1 and H1 were dialyzed overnight in protein dialysis buffer [20 mM Hepes-KOH (pH 7.5), 200 mM KCl, 7 mM $MgCl_2$, and 2 mM BME]. Arrays were diluted to 60 nM in buffer from the chromatin array assembly [20 mM Hepes-KOH (pH 7.5), 1 mM EDTA, and 2 mM BME]. For each reaction, 10 μl of arrays, 2 μl of H1 (or buffer), and 8 μl of HMGB1 (or buffer) were added to a microcentrifuge tube so that the final buffer is 20 mM Hepes-KOH (pH 7.5), 100 mM KCl, 3.5 mM $MgCl_2$, 0.5 mM EDTA, and 2 mM BME. After 30 min at room temperature, reactions were transferred to a 384-well glass bottom plate (Cellvis), which had been mPEGylated and passivated with BSA according to (*54*). Condensates were allowed to settle in the well for at least 1 hour before imaging with a Plan Apo VC 100×/1.4NA (Nikon) oil immersion objective on a Nikon Ti2 microscope equipped with a CREST-V2 LFOV Spinning Disk (Crest Optics), Celesta Light Engine (Lumencor), with excitation wavelengths 546 or 647 nm and emission filters FF01-595/31 or FF02-685/40 (Semrock) to Image Alexa Fluor 555 or 647, respectively, a 405/488/561/640/750 Dichroic (Crest), a Prime 95B 25-mm sCMOS camera, run using NIS Elements 5.41.01 build 1709 (Nikon). FRAP was achieved with a Opti-Microscan FRAP unit with a 405-nm Reflect/430-800 nm Trans Dual TIRF (FRAP) dichroic and 405-nm laser for photobleaching. Twenty % laser power was used to bleach Alexa Fluor 555–labeled H1, and 15% laser power was used to bleach Alexa Fluor 647–labeled chromatin arrays. Average H1 intensity within the bleached area was measured at 2.5 -s intervals for 2 min. Average chromatin intensity within the bleached area was measured at 10-s intervals for 5 or 10 min. The signal was background subtracted and corrected for photobleaching by measuring the average intensity in an identical area of a condensate in the same field of view that had not been bleached using the following formula

$$\text{CorrectedInt} = \left(\text{BleachInt} - \text{BackgroundInt}\right) / \left(\text{ControlInt} - \text{BackgroundInt}\right)$$

The fluorescence recovery was normalized to both the prebleach intensity and postbleach intensity using the following formula

$$\text{NormalizedInt} = (\text{CorrectedInt} - \text{PostBleachInt}) / (\text{PreBleachInt} - \text{PostBleachInt})$$

The data were then fit to the following one-phase exponential association function in GraphPad Prism to determine the rate and mobile fraction of recovery

$$Y = Y0 + (\text{MobileFraction} - Y0) \times \left[1 - \exp(-K \times x)\right]$$

Supplementary Materials

This PDF file includes:

Figs. S1 to S16

Table S1

REFERENCES AND NOTES

1. Y. Lorch, J. W. LaPointe, R. D. Kornberg, Nucleosomes inhibit the initiation of transcription but allow chain elongation with the displacement of histones. *Cell* **49**, 203–210 (1987).
2. C. R. Clapier, J. Iwasa, B. R. Cairns, C. L. Peterson, Mechanisms of action and regulation of ATP-dependent chromatin-remodelling complexes. *Nat. Rev. Mol. Cell Biol.* **18**, 407–422 (2017).
3. J. D. Anderson, J. Widom, Sequence and position-dependence of the equilibrium accessibility of nucleosomal DNA target sites. *J. Mol. Biol.* **296**, 979–987 (2000).
4. G. A. Armeev, A. S. Kniazeva, G. A. Komarova, M. P. Kirpichnikov, A. K. Shaytan, Histone dynamics mediate DNA unwrapping and sliding in nucleosomes. *Nat. Commun.* **12**, 2387 (2021).
5. S. Bilokapic, M. Strauss, M. Halic, Structural rearrangements of the histone octamer translocate DNA. *Nat. Commun.* **9**, 1330 (2018).
6. S. Bilokapic, M. Strauss, M. Halic, Histone octamer rearranges to adapt to DNA unwrapping. *Nat. Struct. Mol. Biol.* **25**, 101–108 (2018).
7. K. J. Polach, J. Widom, Mechanism of protein access to specific DNA sequences in chromatin: A dynamic equilibrium model for gene regulation. *J. Mol. Biol.* **254**, 130–149 (1995).
8. D. V. Fyodorov, B.-R. Zhou, A. I. Skoultchi, Y. Bai, Emerging roles of linker histones in regulating chromatin structure and function. *Nat. Rev. Mol. Cell Biol.* **19**, 192–206 (2018).
9. J. O. Thomas, A. A. Travers, HMG1 and 2, and related 'architectural' DNA-binding proteins. *Trends Biochem. Sci.* **26**, 167–174 (2001).
10. J. O. Thomas, K. Stott, H1 and HMGB1: Modulators of chromatin structure. *Biochem. Soc. Trans.* **40**, 341–346 (2012).
11. Y. Ogawa, S. Aizawa, H. Shirakawa, M. Yoshida, Stimulation of transcription accompanying relaxation of chromatin structure in cells overexpressing high mobility group 1 protein. *J. Biol. Chem.* **270**, 9272–9280 (1995).
12. S. Aizawa, H. Nishino, K. Saito, K. Kimura, H. Shirakawa, M. Yoshida, Stimulation of transcription in cultured cells by high mobility group protein 1: Essential role of the acidic carboxyl-terminal region. *Biochemistry* **33**, 14690–14695 (1994).
13. B.-G. Ju, V. V. Lunyak, V. Perissi, I. Garcia-Bassets, D. W. Rose, C. K. Glass, M. G. Rosenfeld, A topoisomerase IIß-mediated dsDNA break required for regulated transcription. *Science* **312**, 1798–1802 (2006).
14. S. S. Ner, A. A. Travers, HMG-D, the Drosophila melanogaster homologue of HMG 1 protein, is associated with early embryonic chromatin in the absence of histone H1. *EMBO J.* **13**, 1817–1822 (1994).
15. K. Nightingale, S. Dimitrov, R. Reeves, A. P. Wolffe, Evidence for a shared structural role for HMG1 and linker histones B4 and H1 in organizing chromatin. *EMBO J.* **15**, 548–561 (1996).

16. F. Catez, H. Yang, K. J. Tracey, R. Reeves, T. Misteli, M. Bustin, Network of dynamic interactions between histone H1 and high-mobility-group proteins in chromatin. *Mol. Cell. Biol.* **24**, 4321–4328 (2004).
17. E. Meshorer, D. Yellajoshula, E. George, P. J. Scambler, D. T. Brown, T. Misteli, Hyperdynamic plasticity of chromatin proteins in pluripotent embryonic stem cells. *Dev. Cell* **10**, 105–116 (2006).
18. S. Müller, L. Ronfani, M. E. Bianchi, Regulated expression and subcellular localization of HMGB1, a chromatin protein with a cytokine function. *J. Intern. Med.* **255**, 332–343 (2004).
19. L. Cato, K. Stott, M. Watson, J. O. Thomas, The interaction of HMGB1 and linker histones occurs through their acidic and basic tails. *J. Mol. Biol.* **384**, 1262–1272 (2008).
20. W. An, K. van Holde, J. Zlatanova, The non-histone chromatin protein HMG1 protects linker DNA on the side opposite to that protected by linker histones. *J. Biol. Chem.* **273**, 26289–26291 (1998).
21. T. Bonaldi, G. Längst, R. Strohner, P. B. Becker, M. E. Bianchi, The DNA chaperone HMGB1 facilitates ACF/CHRAC-dependent nucleosome sliding. *EMBO J.* **21**, 6865–6873 (2002).
22. M. Duguet, A. M. de Recondo, A deoxyribonucleic acid unwinding protein isolated from regenerating rat liver. Physical and functional properties. *J. Biol. Chem.* **253**, 1660–1666 (1978).
23. L. Falciola, F. Spada, S. Calogero, G. Längst, R. Voit, I. Grummt, M. E. Bianchi, High mobility group 1 protein is not stably associated with the chromosomes of somatic cells. *J. Cell Biol.* **137**, 19–26 (1997).
24. R. D. Phair, P. Scaffidi, C. Elbi, J. Vecerová, A. Dey, K. Ozato, D. T. Brown, G. Hager, M. Bustin, T. Misteli, Global nature of dynamic protein-chromatin interactions in vivo: Three-dimensional genome scanning and dynamic interaction networks of chromatin proteins. *Mol. Cell. Biol.* **24**, 6393–6402 (2004).
25. P. Scaffidi, T. Misteli, M. E. Bianchi, Release of chromatin protein HMGB1 by necrotic cells triggers inflammation. *Nature* **418**, 191–195 (2002).
26. T. Ueda, H. Chou, T. Kawase, H. Shirakawa, M. Yoshida, Acidic C-tail of HMGB1 is required for its target binding to nucleosome linker DNA and transcription stimulation. *Biochemistry* **43**, 9901–9908 (2004).
27. A. E. White, A. R. Hieb, K. Luger, A quantitative investigation of linker histone interactions with nucleosomes and chromatin. *Sci. Rep.* **6**, 19122 (2016).
28. M. J. McCauley, E. M. Rueter, I. Rouzina, L. J. Maher III, M. C. Williams, Single-molecule kinetics reveal microscopic mechanism by which high-mobility group B proteins alter DNA flexibility. *Nucleic Acids Res.* **41**, 167–181 (2013).
29. P. O. Heidarsson, D. Mercadante, A. Sottini, D. Nettels, M. B. Borgia, A. Borgia, S. Kilic, B. Fierz, R. B. Best, B. Schuler, Release of linker histone from the nucleosome driven by polyelectrolyte competition with a disordered protein. *Nat. Chem.* **14**, 224–231 (2022).
30. L. C. Bryan, D. R. Weilandt, A. L. Bachmann, S. Kilic, C. C. Lechner, P. D. Odermatt, G. E. Fantner, S. Georgeon, O. Hantschel, V. Hatzimanikatis, B. Fierz, Single-molecule kinetic analysis of HP1-chromatin binding reveals a dynamic network of histone modification and DNA interactions. *Nucleic Acids Res.* **45**, 10504–10517 (2017).
31. B.-R. Zhou, H. Feng, H. Kato, L. Dai, Y. Yang, Y. Zhou, Y. Bai, Structural insights into the histone H1-nucleosome complex. *Proc. Natl. Acad. Sci. U.S.A.* **110**, 19390–19395 (2013).
32. F. Song, P. Chen, D. Sun, M. Wang, L. Dong, D. Liang, R.-M. Xu, P. Zhu, G. Li, Cryo-EM study of the chromatin fiber reveals a double helix twisted by tetranucleosomal units. *Science* **344**, 376–380 (2014).
33. J. Bednar, I. Garcia-Saez, R. Boopathi, A. R. Cutter, G. Papai, A. Reymer, S. H. Syed, I. N. Lone, O. Tonchev, C. Crucifix, H. Menoni, C. Papin, D. A. Skoufias, H. Kurumizaka, R. Lavery, A. Hamiche, J. J. Hayes, P. Schultz, D. Angelov, C. Petosa, S. Dimitrov, Structure and dynamics of a 197 bp nucleosome in complex with linker histone H1. *Mol. Cell* **66**, 384–397.e8 (2017).
34. S. Knapp, S. Müller, G. Digilio, T. Bonaldi, M. E. Bianchi, G. Musco, The long acidic tail of high mobility group box 1 (HMGB1) protein forms an extended and flexible structure that interacts with specific residues within and between the hmg boxes. *Biochemistry* **43**, 11992–11997 (2004).
35. K. Stott, M. Watson, F. S. Howe, J. G. Grossmann, J. O. Thomas, Tail-mediated collapse of HMGB1 is dynamic and occurs *via* differential binding of the acidic tail to the A and B domains. *J. Mol. Biol.* **403**, 706–722 (2010).
36. M. Watson, K. Stott, J. O. Thomas, Mapping intramolecular interactions between domains in HMGB1 using a tail-truncation approach. *J. Mol. Biol.* **374**, 1286–1297 (2007).
37. M. J. McCauley, J. Zimmerman, L. J. Maher, M. C. Williams, HMGB binding to DNA: Single and double box motifs. *J. Mol. Biol.* **374**, 993–1004 (2007).
38. T. Kawase, K. Sato, T. Ueda, M. Yoshida, Distinct domains in HMGB1 are involved in specific intramolecular and nucleosomal interactions. *Biochemistry* **47**, 13991–13996 (2008).
39. M. Watson, K. Stott, H. Fischl, L. Cato, J. O. Thomas, Characterization of the interaction between HMGB1 and H3—A possible means of positioning HMGB1 in chromatin. *Nucleic Acids Res.* **42**, 848–859 (2014).
40. A. Agresti, M. E. Bianchi, HMGB proteins and gene expression. *Curr. Opin. Genet. Dev.* **13**, 170–178 (2003).
41. A. A. Travers, Priming the nucleosome: A role for HMGB proteins? *EMBO Rep.* **4**, 131–136 (2003).
42. M. J. McCauley, R. Huo, N. Becker, M. N. Holte, U. M. Muthurajan, I. Rouzina, K. Luger, L. J. Maher, N. E. Israeloff, M. C. Williams, Single and double box HMGB proteins differentially destabilize nucleosomes. *Nucleic Acids Res.* **47**, 666–678 (2019).
43. A. Ragab, A. Travers, HMG-D and histone H1 alter the local accessibility of nucleosomal DNA. *Nucleic Acids Res.* **31**, 7083–7089 (2003).
44. S. O. Dodonova, F. Zhu, C. Dienemann, J. Taipale, P. Cramer, Nucleosome-bound SOX2 and SOX11 structures elucidate pioneer factor function. *Nature* **580**, 669–672 (2020).
45. M. Ghoneim, H. A. Fuchs, C. A. Musselman, Histone tail conformations: A fuzzy affair with DNA. *Trends Biochem. Sci.* **46**, 564–578 (2021).
46. K. J. Polach, P. T. Lowary, J. Widom, Effects of core histone tail domains on the equilibrium constants for dynamic dna site accessibility in nucleosomes1. *J. Mol. Biol.* **298**, 211–223 (2000).
47. R. Sánchez-Giraldo, F. J. Acosta-Reyes, C. S. Malarkey, N. Saperas, M. E. A. Churchill, J. L. Campos, Two high-mobility group box domains act together to underwind and kink DNA. *Acta Cryst. D* **71**, 1423–1432 (2015).
48. K. Stott, G. S. F. Tang, K.-B. Lee, J. O. Thomas, Structure of a complex of tandem HMG boxes and DNA. *J. Mol. Biol.* **360**, 90–104 (2006).
49. S.-H. Teo, K. D. Grasser, J. O. Thomas, Differences in the DNA-binding properties of the Hmg-box domains of HMG1 and the sex-determining factor SRY. *Eur. J. Biochem.* **230**, 943–950 (1995).
50. E. D. Zhong, T. Bepler, B. Berger, J. H. Davis, CryoDRGN: Reconstruction of heterogeneous cryo-EM structures using neural networks. *Nat. Methods* **18**, 176–185 (2021).
51. S. H. Syed, D. Goutte-Gattat, N. Becker, S. Meyer, M. S. Shukla, J. J. Hayes, R. Everaers, D. Angelov, J. Bednar, S. Dimitrov, Single-base resolution mapping of H1–nucleosome interactions and 3D organization of the nucleosome. *Proc. Natl. Acad. Sci. U.S.A.* **107**, 9620–9625 (2010).
52. N. J. Abdulhay, C. P. McNally, L. J. Hsieh, S. Kasinathan, A. Keith, L. S. Estes, M. Karimzadeh, J. G. Underwood, H. Goodarzi, G. J. Narlikar, V. Ramani, Massively multiplex single-molecule oligonucleosome footprinting. *eLife* **9**, e59404 (2020).
53. N. J. Abdulhay, L. J. Hsieh, C. P. McNally, M. S. Ostrowski, C. M. Moore, M. Ketavarapu, S. Kasinathan, A. S. Nanda, K. Wu, U. S. Chio, Z. Zhou, H. Goodarzi, G. J. Narlikar, V. Ramani, Nucleosome density shapes kilobase-scale regulation by a mammalian chromatin remodeler. *Nat. Struct. Mol. Biol.* **30**, 1571–1581 (2023).
54. B. A. Gibson, L. K. Doolittle, M. W. G. Schneider, L. E. Jensen, N. Gamarra, L. Henry, D. W. Gerlich, S. Redding, M. K. Rosen, Organization of chromatin by intrinsic and regulated phase separation. *Cell* **179**, 470–484.e21 (2019).
55. T. T. M. Ngo, Q. Zhang, R. Zhou, J. G. Yodh, T. Ha, Asymmetric unwrapping of nucleosomes under tension directed by DNA local flexibility. *Cell* **160**, 1135–1144 (2015).
56. P. J. J. Robinson, L. Fairall, V. A. T. Huynh, D. Rhodes, EM measurements define the dimensions of the "30-nm" chromatin fiber: Evidence for a compact, interdigitated structure. *Proc. Natl. Acad. Sci. U.S.A.* **103**, 6506–6511 (2006).
57. A. Balliano, F. Hao, C. Njeri, L. Balakrishnan, J. J. Hayes, HMGB1 stimulates activity of polymerase β on nucleosome substrates. *Biochemistry* **56**, 647–656 (2017).
58. M. I. Hepp, V. Alarcon, A. Dutta, J. L. Workman, J. L. Gutiérrez, Nucleosome remodeling by the SWI/SNF complex is enhanced by yeast high mobility group box (HMGB) proteins. *Biochim. Biophys. Acta* **1839**, 764–772 (2014).
59. S. R. Joshi, Y. C. Sarpong, R. C. Peterson, W. M. Scovell, Nucleosome dynamics: HMGB1 relaxes canonical nucleosome structure to facilitate estrogen receptor binding. *Nucleic Acids Res.* **40**, 10161–10171 (2012).
60. I. Ugrinova, I. G. Pashev, E. A. Pasheva, Nucleosome binding properties and co-remodeling activities of native and in vivo acetylated HMGB-1 and HMGB–2 proteins. *Biochemistry* **48**, 6502–6507 (2009).
61. D. D. Winkler, K. Luger, The histone chaperone FACT: Structural insights and mechanisms for nucleosome reorganization. *J. Biol. Chem.* **286**, 18369–18374 (2011).
62. B. Celona, A. Weiner, F. Di Felice, F. M. Mancuso, E. Cesarini, R. L. Rossi, L. Gregory, D. Baban, G. Rossetti, P. Grianti, M. Pagani, T. Bonaldi, J. Ragoussis, N. Friedman, G. Camilloni, M. E. Bianchi, A. Agresti, Substantial histone reduction modulates genomewide nucleosomal occupancy and global transcriptional output. *PLoS Biol.* **9**, e1001086 (2011).
63. S. S. Lange, D. L. Mitchell, K. M. Vasquez, High mobility group protein B1 enhances DNA repair and chromatin modification after DNA damage. *Proc. Natl. Acad. Sci. U.S.A.* **105**, 10320–10325 (2008).
64. T. Osmanov, I. Ugrinova, E. Pasheva, The chaperone like function of the nonhistone protein HMGB1. *Biochem. Biophys. Res. Commun.* **432**, 231–235 (2013).
65. N. Patenge, S. K. Elkin, M. A. Oettinger, ATP-dependent remodeling by SWI/SNF and ISWI proteins stimulates V(D)J cleavage of 5 S arrays. *J. Biol. Chem.* **279**, 35360–35367 (2004).
66. V. Boonyaratanakornkit, V. Melvin, P. Prendergast, M. Altmann, L. Ronfani, M. E. Bianchi, L. Taraseviciene, S. K. Nordeen, E. A. Allegretto, D. P. Edwards, High-mobility group chromatin proteins 1 and 2 functionally interact with steroid hormone receptors to enhance their DNA binding in vitro and transcriptional activity in mammalian cells. *Mol. Cell. Biol.* **18**, 4471–4487 (1998).

67. D. Das, R. C. Peterson, W. M. Scovell, High mobility group B proteins facilitate strong estrogen receptor binding to classical and half-site estrogen response elements and relax binding selectivity. *Mol. Endocrinol.* **18**, 2616–2632 (2004).
68. M. Decoville, M. J. Giraud-Panis, C. Mosrin-Huaman, M. Leng, D. Locker, HMG boxes of DSP1 protein interact with the Rel homology domain of transcription factors. *Nucleic Acids Res.* **28**, 454–462 (2000).
69. L. Jayaraman, N. C. Moorthy, K. G. K. Murthy, J. L. Manley, M. Bustin, C. Prives, High mobility group protein-1 (HMG-1) is a unique activator of p53. *Genes Dev.* **12**, 462–472 (1998).
70. S. R. Joshi, R. B. Ghattamaneni, W. M. Scovell, Expanding the paradigm for estrogen receptor binding and transcriptional activation. *Mol. Endocrinol.* **25**, 980–994 (2011).
71. S. A. Oñate, P. Prendergast, J. P. Wagner, M. Nissen, R. Reeves, D. E. Pettijohn, D. P. Edwards, The DNA-bending protein HMG-1 enhances progesterone receptor binding to its target DNA sequences. *Mol. Cell. Biol.* **14**, 3376–3391 (1994).
72. V. Zappavigna, L. Falciola, M. Helmer-Citterich, F. Mavilio, M. E. Bianchi, HMG1 interacts with HOX proteins and enhances their DNA binding and transcriptional activation. *EMBO J.* **15**, 4981–4991 (1996).
73. S. Zwilling, H. König, T. Wirth, High mobility group protein 2 functionally interacts with the POU domains of octamer transcription factors. *EMBO J.* **14**, 1198–1208 (1995).
74. K. Sofiadis, N. Josipovic, M. Nikolic, Y. Kargapolova, N. Übelmesser, V. Varamogianni-Mamatsi, A. Zirkel, I. Papadionysiou, G. Loughran, J. Keane, A. Michel, E. G. Gusmao, C. Becker, J. Altmüller, T. Georgomanolis, A. Mizi, A. Papantonis, HMGB1 coordinates SASP-related chromatin folding and RNA homeostasis on the path to senescence. *Mol. Syst. Biol.* **17**, e9760 (2021).
75. A. Contreras, T. K. Hale, D. L. Stenoien, J. M. Rosen, M. A. Mancini, R. E. Herrera, The dynamic mobility of histone H1 Is regulated by Cyclin/CDK phosphorylation. *Mol. Cell. Biol.* **23**, 8626–8636 (2003).
76. R. N. Bhattacharjee, G. C. Banks, K. W. Trotter, H.-L. Lee, T. K. Archer, Histone H1 phosphorylation by Cdk2 selectively modulates mouse mammary tumor virus transcription through chromatin remodeling. *Mol. Cell. Biol.* **21**, 5417–5425 (2001).
77. Y. Dou, C. A. Mizzen, M. Abrams, C. D. Allis, M. A. Gorovsky, Phosphorylation of linker histone H1 regulates gene expression in vivo by mimicking H1 removal. *Mol. Cell* **4**, 641–647 (1999).
78. Y. Dou, M. A. Gorovsky, Phosphorylation of linker histone H1 regulates gene expression in vivo by creating a charge patch. *Mol. Cell* **6**, 225–231 (2000).
79. Y. Arimura, R. M. Shih, R. Froom, H. Funabiki, Structural features of nucleosomes in interphase and metaphase chromosomes. *Mol. Cell* **81**, 4377–4397.e12 (2021).
80. S. Cai, Y. Song, C. Chen, J. Shi, L. Gan, Natural chromatin is heterogeneous and self-associates in vitro. *Mol. Biol. Cell* **29**, 1652–1663 (2018).
81. S. Cai, C. Chen, Z. Y. Tan, Y. Huang, J. Shi, L. Gan, Cryo-ET reveals the macromolecular reorganization of *S. pombe* mitotic chromosomes in vivo. *Proc. Natl. Acad. Sci. U.S.A.* **115**, 10977–10982 (2018).
82. S. Cai, D. Böck, M. Pilhofer, L. Gan, The in situ structures of mono-, di-, and trinucleosomes in human heterochromatin. *Mol. Biol. Cell* **29**, 2450–2457 (2018).
83. Z. Y. Tan, S. Cai, A. J. Noble, J. K. Chen, J. Shi, L. Gan, Heterogeneous non-canonical nucleosomes predominate in yeast cells in situ. *eLife* **12**, RP87672 (2023).
84. K. Luger, T. J. Rechsteiner, T. J. Richmond, Preparation of nucleosome core particle from recombinant histones. *Methods Enzymol.* **304**, 3–19 (1999).
85. S. Q. Zheng, E. Palovcak, J.-P. Armache, K. A. Verba, Y. Cheng, D. A. Agard, MotionCor2: Anisotropic correction of beam-induced motion for improved cryo-electron microscopy. *Nat. Methods* **14**, 331–332 (2017).
86. A. Punjani, J. L. Rubinstein, D. J. Fleet, M. A. Brubaker, cryoSPARC: Algorithms for rapid unsupervised cryo-EM structure determination. *Nat. Methods* **14**, 290–296 (2017).
87. D. Asarnow, E. Palovcak, Y. Cheng, asarnow/pyem: UCSF pyem v0.5, version v0.5, Zenodo (2019); https://doi.org/10.5281/zenodo.3576630.
88. S. H. W. Scheres, RELION: Implementation of a Bayesian approach to cryo-EM structure determination. *J. Struct. Biol.* **180**, 519–530 (2012).
89. U. S. Chio, E. Palovcak, A. A. A. Smith, H. Autzen, E. N. Muñoz, Z. Yu, F. Wang, D. A. Agard, J.-P. Armache, G. J. Narlikar, Y. Cheng, Functionalized graphene-oxide grids enable high-resolution cryo-EM structures of the SNF2h-nucleosome complex without crosslinking. *Nat. Commun.* **15**, 2225 (2024).
90. T. I. Croll, ISOLDE: A physically realistic environment for model building into low-resolution electron-density maps. *Acta Cryst. D* **74**, 519–530 (2018).
91. H. Li, Minimap2: Pairwise alignment for nucleotide sequences. *Bioinformatics* **34**, 3094–3100 (2018).

Acknowledgments: We thank J. Tretyakova for purification of all histones used in this manuscript. We thank M. K. Rosen for the H1.4 and H1.4-ΔCTE expression plasmids. We thank S. Y. Kim for tireless help and advice on condensate microscopy experiments. We thank K. Herrington, the UCSF Center for Advanced Light Microscopy, and the Nikon Imaging Center for access to tools and expertise for microscopy experiments. We thank J. D. Gross and D. Galonić Fujimori for thorough advice throughout this work and helpful comments on preparation of the manuscript. We thank all members of the Narlikar Lab for stimulating discussion of this project at all stages. **Funding:** This work was supported by grants from the National Institutes of Health to G.J.N. (R35GM127020), to V.R. (DP2-HG012442), to G.J.N. and V.R. (U01-DK127421), to Y.C. (R35GM140847), and to U.S.C. (F32GM137463). Y.C. is an investigator of the Howard Hughes Medical Institute. Equipment at the UCSF cryo-EM facility was partially supported by the NIH (grants S10OD020054, S10OD021741, and S10OD025881). Portions of this work were funded through the gracious support of the UCSF Program for Breakthrough Biomedical Research and the Sandler Fellows program. **Author contributions:** Conceptualization: H.S.S. and G.J.N. Methodology: H.S.S., U.S.C., and G.J.N. Validation: H.S.S. and G.J.N. Formal analysis: H.S.S. and U.S.C. Investigation: H.S.S., U.S.C., and C.M.M. Resources: H.S.S. and G.J.N. Data curation: U.S.C. Writing—original draft: H.S.S. and G.J.N. Writing—review and editing: H.S.S., U.S.C., C.M.M., V.R., Y.C., and G.J.N. Visualization: H.S.S., U.S.C., and C.M.M. Supervision: Y.C., V.R., and G.J.N. Project administration: H.S.S., V.R., and G.J.N. Funding acquisition: Y.C., V.R., and G.J.N. **Competing interests:** Y.C. is a scientific advisory board member of ShuiMu BioSciences. G.J.N. is a founder and scientific advisory board member of TippingPoint Biosciences. All other authors declare that they have no competing interests. **Data and materials availability:** For the structure of HMGB1 bound to 0/10 nucleosomes at SHL −2, the coordinates are deposited in the Protein Data Bank with accession code 9CG9; the cryo-EM density map is deposited in the Electron Microscopy Data Bank (EMDB) with the accession code EMD-45578. All data needed to evaluate the conclusions in the paper are present in the paper and/or the Supplementary Materials.

Submitted 18 November 2024
Accepted 15 July 2025
Published 15 August 2025
10.1126/sciadv.ads4473